Monthly Notices of the ROYAL ASTRONOMICAL SOCIETY

MNRAS **540,** 2727–2744 (2025) https://doi.org/10.1093/mnras/staf892
Advance Access publication 2025 May 31

Prompt periodicity in the GRB 211211A precursor: black-hole or magnetar engine?

Gavin P. Lamb [1]★ Thomas Baxter [1] Conor M. B. Omand [1] Dimple [2] Zoë McGrath [1] Cairns Turnbull [1] Eric Burns [3] Hamid Hamidani [4] Ilya Mandel [5,6] Kim L. Page [7] Stephan Rosswog [8,9] Nikhil Sarin [9,10] Andrew Blain [6] Laurence Datrier [11] Shiho Kobayashi [1] Andrew Levan [12] Rhaana Starling [7] Benjamin Gompertz [2] Nusrin Habeeb,[7] Khang Nguyen[1] and Nial Tanvir [7]

[1]*Astrophysics Research Institute, Liverpool John Moores University, IC2 Liverpool Science Park, 146 Brownlow Hill, Liverpool L3 5RF, UK*
[2]*School of Physics and Astronomy, University of Birmingham, Edgbaston, Birmingham B15 2TT, UK*
[3]*Department of Physics and Astronomy, Louisiana State University, Baton Rouge, LA 70803, USA*
[4]*Astronomical Institute, Graduate School of Science, Tohoku University, 6-3, Aramaki Aza-Aoba, Aoba-ku, Sendai 980-8578, Japan*
[5]*School of Physics and Astronomy, Monash University, Wellington Road, Clayton, Victoria 3800, Australia*
[6]*ARC Centre of Excellence for Gravitational Wave Discovery – OzGrav, Level 9, AMDC Building Swinburne University of Technology, Hawthorn VIC 3122, Australia*
[7]*School of Physics and Astronomy, University of Leicester, University Road, Leicester LE1 7RH, UK*
[8]*Hamburger Sternwarte, University of Hamburg, Gojenbergsweg 112, D-21029 Hamburg, Germany*
[9]*The Oskar Klein Centre, Department of Physics, Stockholm University, AlbaNova, Roslagstullsbacken 21, SE-106 91 Stockholm, Sweden*
[10]*Nordita, Stockholm University and KTH Royal Institute of Technology Hannes Alfvéns väg 12, SE-106 91 Stockholm, Sweden*
[11]*California State University, Fullerton, Department of Physics, 800 N State College Blvd, Fullerton, CA 92831, USA*
[12]*Institute for Mathematics, Astrophysics and Particle Physics, Department of Astrophysics, Radboud University, Heyendaalseweg 135, 6525 AJ Nijmegen, Gelderland, NL*

Accepted 2025 May 29. Received 2025 May 22; in original form 2025 March 19

ABSTRACT

The merger origin long GRB 211211A was a class (re-)defining event. A precursor was identified with a ~ 1 s separation from the main burst, as well as a claimed candidate quasi-periodic oscillation (QPO) with a frequency ~ 20 Hz. Here, we explore the implications of the precursor, assuming the quasi-periodicity is real. The precursor variability time-scale requires relativistic motion with a Lorentz factor $\Gamma \gtrsim 80$, and implies an engine-driven jetted outflow. The declining amplitude of the consecutive pulses requires an episodic engine with an 'on/off' cycle consistent with the QPO. For a black-hole central engine, the QPO can have its origin in Lense–Thirring precession of the inner disc at ~ 6–$9\,r_g$ (gravitational radii) for a mass $M_\bullet \leq 4.5\,\mathrm{M}_\odot$, and $\lesssim 7\,r_g$ for $M_\bullet > 4.5\,\mathrm{M}_\odot$ and dimensionless spin $\chi \sim 0.3$–0.9. Alternatively, at a disc density of $\sim 10^{8-12}\,\mathrm{g\,cm^{-3}}$, the required magnetic field strength for a QPO via magnetohydrodynamic effects will be of the order of $B \sim 10^{12-14}$ G. If the central engine is a short-lived magnetar or hypermassive neutron star, then a low-frequency QPO can be produced via instabilities within the disc at a radius of ~ 20–70 km, for a disc density $\sim 10^{9-12}\,\mathrm{g\,cm^{-3}}$ and magnetic field $\gtrsim 10^{13-14}$ G. The QPO cannot be coupled to the neutron star spin, as the co-rotation radius is beyond the scale of the disc. Neither engine can be ruled out – however, we favour an origin for the precursor candidate QPO as early jet–disc coupling for a neutron star–black hole merger remnant with mass $M_\bullet > 4.5\,\mathrm{M}_\odot$.

Key words: stars: black holes – gamma-ray burst: individual: GRB 211211A – stars: magnetars.

1 INTRODUCTION

Gamma-ray bursts (GRBs) are characteristically high-energy events with very short variability time-scales. The combination of high luminosity and short variability requires these sources to have ultra-relativistic velocities $\Gamma \gg 10$, with Lorentz factors typically of the order of $\Gamma \sim 100$ considered.

The prompt GRB emission light curves can be separated into one or more pulses (e.g. Norris et al. 1996; Kobayashi, Piran & Sari 1997; Norris et al. 2005). Beyond these short time-scale variations, there are three main phases identified within the GRB prompt emission (e.g. Hu et al. 2014): a precursor (Koshut et al. 1995); the main burst complex; and extended, plateau, and late-flaring

★ E-mail: g.p.lamb@ljmu.ac.uk

emission (Burrows et al. 2005). While the main phase is usually the most energetic and well-studied, precursors (short bursts of radiation occurring before the main event) have been a compelling component of GRB prompt emission (Koshut et al. 1995; Lazzati 2005; Burlon et al. 2008, 2009; Hu et al. 2014; Zhong et al. 2019; Coppin, de Vries & van Eijndhoven 2020; Li et al. 2021; Li & Mao 2022), with many competing explanations. These include pair cascades producing a quasi-thermal X-ray pulse (Mészáros, Ramirez-Ruiz & Rees 2001); shock or cocoon breakout from the stellar envelope or merger ejecta (Ramirez-Ruiz, Celotti & Rees 2002; Nakar & Piran 2017); 'spinar-like object' due to a two phase core collapse (Lipunova et al. 2009); a central engine origin that is the same as the main burst complex, for short GRB precursors (Troja, Rosswog & Gehrels 2010); distinct fireballs with their own afterglow (Nappo et al. 2014); crustal resonances and shattering in pre-merger neutron stars (Tsang et al. 2012; Suvorov & Kokkotas 2020; Neill et al. 2022); g-mode oscillations in pre-merger neutron stars (Kuan, Suvorov & Kokkotas 2021); changes in the energy content of the early jet, baryonic to Poynting flux dominated (Wang et al. 2020); etc.

The main burst complex is used to classify GRBs via their observed duration; short (< 2 s) and long (> 2 s) (Kouveliotou et al. 1993); alternatively, schemes put GRBs into two categories – Type I and Type II (Zhang et al. 2009). For GRB precursors, there is a distinction between those from Type I (typically short-duration GRBs) and those from Type II (typically long-duration GRBs). The latter are well fit with a thermal spectrum and exhibit a smoother light curve (e.g. Wang et al. 2007; Gutiérrez et al. 2025), whereas the former are typically consistent with the emission qualities of the main burst complex (e.g. Troja et al. 2010).

Among the GRB population are several events that challenge the established classification schemes; the most prominent and convincing of these is GRB 211211A (Gompertz et al. 2023). Despite its long duration [51 or 34.3 s for *Fermi*-Gamma Burst Monitor (GBM) and *Swift*-Burst Alert Telescope (BAT), respectively], the burst was accompanied by a candidate kilonova, seen within the afterglow (Rastinejad et al. 2022). A kilonova is a thermal transient produced via neutron star mergers and is the observational smoking gun for a merger origin of GRBs (see Metzger 2020, for a review of kilonova). At the time of discovery, this kilonova was the best-sampled example of such a transient within the afterglow of a classical GRB – the kilonova following the neutron star merger GW170817 being the best sampled kilonova case; however, GRB 170817A was far from typical/classical in terms of the GRB population (see Abbott et al. 2017, for the discovery paper).

The afterglow, candidate kilonova, candidate host galaxy, and the prompt emission were thoroughly investigated (e.g. Gao, Lei & Zhu 2022; Mei et al. 2022; Rastinejad et al. 2022; Yang et al. 2022; Zhang et al. 2022; Zhu et al. 2022; Chang et al. 2023; Gompertz et al. 2023; Hamidani et al. 2024; Waxman, Ofek & Kushnir 2025). Compounding the uniqueness of GRB 211211A, the burst had a short ($\sim$0.2 s) precursor with an isotropic equivalent energy, $E_{\rm pre,iso} \sim 7 \times 10^{48}$ erg, which exhibited apparent periodicity, with claims for a quasi-periodic oscillation (QPO) at ~ 22 Hz (Xiao et al. 2024). A further QPO candidate within the main burst complex, again lasting ~ 0.2 s, was claimed by Chirenti et al. (2024); however, their analysis found the precursor QPO claimed by Xiao et al. (2024) to be below their levels of significance. We note that Xiao et al. (2024) performed multiple significance tests for the QPO, and found it to be significant by all measures.

Several progenitor models have been proposed to explain the origin of GRB 211211A: a neutron star–white dwarf merger with a rapidly spinning magnetar remnant (Yang et al. 2022; Fan et al. 2024); resonances within neutron star oceans (Sullivan et al. 2024); a neutron star–black hole or binary neutron star merger (Zhu et al. 2022; Barnes & Metzger 2023; Dimple, Misra & Arun 2023; Kunert et al. 2024). Notably, QPOs have been suggested as an indicator of neutron star–black hole merger remnants (Stone, Loeb & Berger 2013; Li, Shen & Zhang 2023).

The candidate QPO in the precursor of GRB 211211A presents a unique opportunity to probe the mechanisms driving the early phases of GRB emission related to accretion and jet launching. QPOs have been observed in various astrophysical systems; however, their presence in GRBs is rare and provides hints to the nature of the central engine (see Chirenti et al. 2023 for the discovery of two QPOs within legacy catalogues of short-duration bursts GRB 910 711 and 931101B, and Yang et al. 2025 for further high-frequency discoveries within short GRBs). For the kilo-Hertz frequency QPOs in GRBs 910 711 and 931101B, the origin aligns well with the expectation from neutron star mergers, and Guedes et al. (2025) have proposed using this to constrain the burst redshift and infer the mass–radius relation of the neutron stars. Our study reinvestigates the precursor and candidate, low-frequency QPO of GRB 211211A, with an aim to characterize its properties and to explore its physical origin.

For binary neutron star mergers, several mechanisms exist that can produce precursor-like emission before the merger (Fernández & Metzger 2016). These include magnetospheric interactions between the two neutron stars; however, these are predicted to produce flares with a maximum luminosity of $L \leq 10^{44}\,{\rm erg\,s^{-1}}$ (Wang et al. 2018), several orders of magnitude fainter than the GRB 211211A precursor. An alternative to magnetospheric interactions is resonant shattering flares (Tsang et al. 2012), where the tidal interactions between the pre-merger neutron stars can produce a resonance sufficient to shatter the crust, leading to a series of ejected shells that can collide to produce internal shocks similar to those of the GRB prompt emission but of the order of $L \leq 10^{48}\,{\rm erg\,s^{-1}}$ (Neill et al. 2022). However, the candidate QPO frequency and the temporal structure of the GRB 211211A precursor are inconsistent with such resonant shattering flares (see the addendum within Neill et al. 2022). A second long-duration merger origin burst, GRB 230307A (Levan et al. 2024), also contained a potential precursor. The resonant shattering flare scenario was invoked to explain this emission, despite the candidate precursor's relatively high luminosity (for a precursor) – by invoking high magnetic field strengths, Dichiara et al. (2023) were able to find a viable parameter space in this case. The high magnetic field strengths would require one of the merging components to be a magnetar. While magnetar lifetime is typically considered to be shorter than the neutron star merger timescale, there is some evidence of an old population of magnetars (Beniamini et al. 2023). A final precursor model for GRB 211211A invokes the merger of a black hole and a massive neutron star, producing tidal resonances that can produce the observed precursor yet struggles to explain the main burst complex or kilonova (Sullivan et al. 2024). For GRB 211211A, the various pre-merger flare models can be ruled out due to the luminosity or the temporal structure of the precursor.

We do not attempt to confirm the significance of the candidate QPO within the precursor of GRB 211211A, but rather explore viable mechanisms for such a QPO given a compact merger origin for the GRB. Robust tests for the significance of a QPO could involve Gaussian process modelling (Hübner et al. 2022) – such a test is beyond the scope of this work, and has some overlap with the methods employed by Xiao et al. (2024) in their discovery paper.

We first discuss potential origins for a QPO in a post-merger system in Section 2. The data used in our search for the candidate QPO are described in Section 3, and the results of the data analysis are given in Section 4. The results are discussed in the context of an accreting compact object and the various mechanisms explored in Section 5, and our conclusions are made in Section 6.

2 POTENTIAL QPO ORIGINS

For GRBs, accretion on to a newly formed stellar mass black hole, or a magnetar (magnetized neutron star), is the most likely engine for jetted emission (see e.g. Fryer et al. 2019). For these scenarios, the exact nature of the progenitor system is not exclusive. For instance, a magnetar system for GRB 211211A could result from a neutron-star merger or a white-dwarf–neutron star merger (e.g. Yang et al. 2022). Similarly, a black-hole engine can be the product of either a neutron star binary or a neutron star black-hole merger.

More exotic but potentially viable models would also fall under one of these two categories. For example, consider white dwarf–black hole mergers; although unlikely to produce a GRB (Narayan, Piran & Kumar 2001), if they did, they would follow a black-hole accretion scenario. In another case, quark stars, if produced from a neutron star merger, would follow either a black-hole or magnetar scenario, depending on the specific properties of the quark stars (Cheng & Dai 1996).

Meanwhile, even more exotic progenitor systems can be safely ruled out, as the origin of the prompt emission, due to the phenomenology and properties of GRB 211211A. Soft gamma repeaters and magnetar giant flares, for instance, are extremely short in duration and have a local Universe origin. Primordial black hole evaporation is expected to result in a thermal short-duration GRB with an origin within a few parsecs (Cline & Hong 1992). Finally, nuclear goblins (probably) do not exist (Zwicky 1974).

Here, we outline possible mechanisms for generating QPOs with such engines.

2.1 Black-hole accretion

For black-hole accretion disc systems, there are several potential origins for QPOs in the emission. Oscillation within the precursor implies that the engine exhibits periodicity at very early times.

2.1.1 *Lense–Thirring precession*

Lense–Thirring (LT) precession is the result of frame dragging within the disc of a black hole with spin $\chi > 0$. The frequency of the LT precession is given by (Bardeen & Petterson 1975; Kumar & Pringle 1985):

$$\nu_{\rm LT} = \frac{\omega_{\rm LT}}{2\pi} = \frac{\chi G^2 M_\bullet^2}{\pi c^3 r_{\rm id}^3}, \tag{1}$$

where χ is the dimensionless spin of the black hole, $M_\bullet$ is the black-hole mass, c is the speed of light, G is the gravitational constant, and $r_{\rm id}$ is the inner radius of the accretion disc. In the following text we will always assume that the disc mass is negligible with respect to the central mass, which should be a reasonable approximation.

2.1.2 *Discoseismology: p and g modes*

Pressure and gravity modes of buoyancy waves trapped within a black-hole accretion disc can result in a QPO (Kato & Fukue 1980; Wagoner 1999). The inertial acoustic, or pressure modes (p modes), where pressure is the restoring force, have oscillation frequencies of

$$\nu_{\rm p-mode} \simeq \frac{1}{2\pi}\sqrt{\frac{GM_\bullet}{r^3}} = \frac{\omega_{\rm K}(r)}{2\pi} \equiv \nu_{\rm K}(r), \tag{2}$$

where we have denoted the Kepler angular frequency as

$$\omega_{\rm K}(r) = \sqrt{\frac{GM_\bullet}{r^3}}. \tag{3}$$

And gravity modes (g modes), where gravity is the restoring force, have frequencies

$$\nu_{\rm g-mode} \simeq \nu_{\rm p-mode}\frac{N_{BV}}{\kappa}, \tag{4}$$

where N_{BV} is the buoyancy (Brunt–Väisälä) frequency, and κ is the epicyclic (a 'Spirograph'-like motion) frequency.

2.1.3 *Orbital resonance*

When a QPO is related to the orbital, radial, and vertical epicyclic frequencies, these are called orbital resonances (Török & Stuchlík 2005). These characteristic frequencies are

$$\nu_\phi = \nu_{\rm K}(r). \tag{5}$$

The orbital frequency has the same order as the p mode of discoseismology; however, the mechanisms are distinct. Although the p mode is a local oscillation within the disc driven by pressure forces, the orbital resonance is a global phenomenon that couples to fundamental frequencies. This non-linear coupling of fundamental frequencies can produce pairs of QPOs.

The radial and vertical frequencies are then (Kato 2001):

$$\nu_r = \nu_\phi\sqrt{1 - \frac{6GM_\bullet}{rc^2} + \frac{8\chi GM_\bullet^{3/2}}{c^3 r^{3/2}} - \frac{3\chi^2 GM_\bullet^2}{c^4 r^2}}, \tag{6}$$

$$\nu_\theta = \nu_\phi\sqrt{1 - \frac{4\chi GM_\bullet}{r^{3/2}c^2}}, \tag{7}$$

where the epicyclic frequency and orbital frequency have the ratio 3/2, the system is in the 3:2 resonance, and at low frequencies, the QPO can be due to the precession frequency, $\nu_{\rm low} = \nu_\phi - \nu_r$.

2.1.4 *Blobs*

If the disc contains a blob, or hot spot, at a particular radius, there will be an oscillation at the Keplerian frequency, $\nu_{\rm blob} \equiv \nu_\phi$, equation (5).

2.1.5 *Magnetohydrodynamics process*

Magnetohydrodynamic (MHD) turbulence such as magnetorotational instabilities (MRI) can drive QPOs and episodic accretion (Masada et al. 2007; Masada & Shibata 2009). The QPOs will have a frequency given by

$$\nu_{\rm MRI} \simeq \frac{k_\parallel v_A}{2\pi}, \tag{8}$$

where $k_\parallel$ is the wavenumber and v_A is the Alfvén speed (Schekochihin et al. 2009).

2.1.6 Accretion flow shock oscillations

Shocks within the accretion flow can form in the inner disc regions. These shocks will oscillate on the dynamical time-scale such that

$$\nu_{\rm shock} \simeq \nu_{\rm K}(r_{\rm shock}), \tag{9}$$

where $r_{\rm shock}$ is the shock radius. As the oscillations depend on the shock location, the frequency of the oscillation can vary from a few to several hundred Hz (Debnath, Chattopadhyay & Joshi 2024).

2.1.7 Time-scale and damping limits for a black hole – disc QPO

The general precursor temporal structure follows a fast rise with exponential decline (FRED) (Xiao et al. 2024). This FRED structure is usually explained with the rise due to shock emission, and the decline being higher latitude emission. However, here the precursor has oscillations and pulses within the decline.

For LT precession, the short duration of the effect puts limits on the scale of the precessing disc element. By equating the QPO duration with the system coherence time, the size of the disc region that participates in the LT precession can be found by considering the differential precession:

$$\Delta r \simeq \frac{r}{3\nu_{\rm LT}t_{\rm coh}}, \tag{10}$$

where Δr is the size of the disc ring responsible for LT precession and $t_{\rm coh}$ is the coherence time.

Mechanisms that can mediate the damping of oscillations include (see e.g. Armitage 2022, and references therein) viscous damping, disc warping, radiative cooling, magnetic damping, and jet interaction.

Viscous stressing within the precessing disc region will dissipate energy; the time-scale is (King, Pringle & Livio 2007)

$$t_{\rm visc} \simeq \begin{cases} \frac{r^2}{\alpha c_s h} & \text{thin disc,} \\ \frac{r}{\alpha c_s} & \text{thick disc,} \end{cases} \tag{11}$$

where h is the disc scale height, α is the dimensionless viscosity parameter, and $c_s \leq c/\sqrt{3}$ is the sound speed. For the thick disc case, we have assumed $h \simeq r$.

LT precession of the inner disc can additionally result in a warped or torn disc (Nealon, Price & Nixon 2015). The time-scale for damping of an oscillation will be the dynamical time, $t_{\rm dyn} \propto r^{3/2}M_\bullet^{-1/2}$. This is equivalent to the instability growth time-scale, and the resultant warping or tearing will dissipate energy or break up the disc, leading to damping of the QPO amplitude.

For a precession due to a 'blob' which is hot, radiative cooling will reduce the temperature and pressure, resulting in energy dissipation. The time-scale for such radiative cooling is typically equivalent to the dynamical time-scale, $t_{\rm cool} \equiv t_{\rm dyn}$. The dynamical time-scale will be small for our system; however, if the disc is optically thick at early times, then the cooling time-scale will be $t_{\rm cool} > t_{\rm dyn}$.

Interaction between magnetic fields within the disc and the precessing structure can result in magnetic braking or reconnection (Tabone et al. 2022). Either would dissipate energy, with the relevant time-scale being the Alfvén crossing time, $t_{\rm A\times} \sim h/v_A$. However, this time-scale is sensitive to the scale of the magnetic structure.

Where the precessing structure is coupled to the jet, this jet–disc interaction will extract energy. As energy is removed from the disc, the precession will be dampened. The time-scale for this will be comparable to the observed duration, and requires the total jet power to be comparable, or greater than, the power in the disc precession.

The apparent damping of the QPO could be the result of any, or some combination, of these various mechanisms.

2.2 Magnetar engine

Rapidly rotating, newly formed magnetars are commonly invoked as the power source for many high-energy astrophysical transients, particularly where the energy source is ambiguous. For GRBs, short periodic signatures are potential evidence for magnetars as the engine that drives the GRB-producing jet.

2.2.1 Alfvén waves within a magnetosphere

Magnetars have multiple ways to produce QPOs. The initial analysis of the QPO by Xiao et al. (2024) invoked a magnetar process – either pre-merger magnetosphere interactions or crustal oscillations. The most relevant QPO production mechanism for our scenario, where a relatively low oscillation frequency is observed, of the order of ~ 1 to 100 Hz, is via Alfvén waves within the magnetosphere:[1]

$$\nu_{\rm QPO} \simeq \frac{B}{r_A\sqrt{4\pi\rho}}, \tag{12}$$

where r_A is the Alfvén wavelength, B is the magnetic field strength, and ρ is the magnetospheric plasma density. For our scenario, the natural assumption is to make the spin period of the magnetar directly related to the QPO frequency as $\nu_{\rm QPO} \sim 1/P$, where P is the period.

2.2.2 Damping time-scale of Alfvén waves

Alfvén waves will lose energy via transfer to other modes due to non-linear wave–wave interactions. Such non-linear damping is significant in highly turbulent magnetospheres, as expected for a newly formed magnetar following a neutron star merger. The damping time-scale can be approximated as

$$\tau_{\rm nl} \simeq \frac{r_A}{v_A\delta B/B}, \tag{13}$$

where $v_A = B/\sqrt{4\pi\rho}$ is the Alfvén speed, and $0 < \delta B/B \leq 1$ is the fractional amplitude of the Alfvén wave (i.e. the ratio of the Alfvén wave amplitude to the background magnetic field). The damping time-scale for a magnetar with magnetic field $B \sim 10^{14}$ G, plasma density of the order of $\rho \sim 10^{12}\,{\rm g\,cm^{-3}}$, and $\delta B/B \sim 0.22$ will be ~ 0.2 s, on the same order as the precursor. These parameter values are order-of-magnitude estimates given the expectation for these scenarios and demonstrate that the damping time-scale for such a QPO system is consistent with the observed duration.

3 DATA

We reanalysed the time series data for the sub-second precursor within the initial burst complex of GRB 211211A. Our reanalysis aims to identify[2] the quasi-periodic signal identified by Xiao et al.

[1]This process is analogous to the MHD oscillations described for black-hole accretion discs with equation (8).

[2]Rigorous significance testing for this 22.5 Hz QPO was performed via multiple methods by Xiao et al. (2024); we do not present the repetition of that analysis here.

Table 1. Reference labels used throughout for the seven light curve options. The spectral energy range for each light curve and the figures where these data were used.

Label	Energy range (keV)	See figure
Band 1	15–25	[3,4,1]
Band 2	25–50	[3,4]
Band 3	50–100	[3,4]
Band 4	100–350	[3,4]
Low	15–25	[1]
High	25–350	[1,5]
All	15–350	[2,A1,A2]

(2024) in the ~ 0.2 s precursor of the long-duration GRB 211211A. We used publicly available 15–350 keV data of the GRB event from two telescopes in our study. GRB 211211A has a redshift $z = 0.076$ (Rastinejad et al. 2022).

3.1 *Swift*-BAT

We used the standard HEASOFT BATGRBPRODUCT and BATBINEVT tools to extract light curves for the *Swift*-BAT prompt emission over the default energy bands of 15–25, 25–50, 50–100, and 100–350 keV. The data were re-binned to 4 ms bins for convenient short time-scale/higher frequency sampling and to accurately resolve the precursor. We summed all energy channels to create a 'total' energy light curve, in addition to low- and high-energy light curves with ranges 15–25 and 25–350 keV, as well as the default bands, giving seven light curve options (see Table 1).

3.2 *Fermi*-GBM

We used the time-tagged event (TTE) data[3] for n2 and na, the highest signal-to-noise *Fermi*-GBM detectors for GRB 211211A. The TTE data have 128 energy channels with ~ 2 µs precision, and we binned this using the GDT-CORE tools to 4 ms bins. We further divided the data as for *Swift*-BAT into distinct bands listed in Table 1.

4 ANALYSIS AND RESULTS

The data analysis methods for our QPO search, pulse identification, and the results of these analyses follow.

4.1 Data analysis

Our first step in the search for the precursor QPO signal is to pass the data through a periodogram. We initially use a Lomb–Scargle (LS) method (Lomb 1976; Scargle 1982) for inspection of the frequency domain, which reveals any periodicity within the full time series data.

To isolate periodic features temporally, we use a short time Fourier transform (STFT) (e.g. Sejdić, Djurović & Jiang 2009). This method uses a window centred at each time-step to identify any periodicity within each bin and output a time-series power spectral density (PSD).

4.1.1 Lomb–Scargle

We limit the data to the precursor within a window of -0.03 to 0.22 s either side of the *Fermi*-GBM trigger time. The selected data are detrended using a constant for the 0.25 s window of the precursor.[4] To ensure the time window is consistent between the instruments, BAT and GBM, we overplot the light curves and adjust the zero-time on the BAT data to match the bin-centroid time stamps of the *Fermi*-GBM data. The LS periodogram for the 'low' and 'high' bands is shown in Fig. 1.

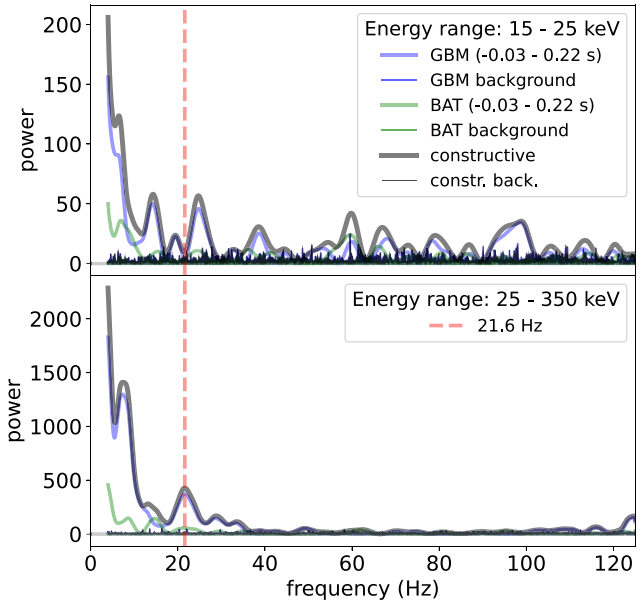

Figure 1. LS periodogram of the 4 ms binned and detrended precursor data between -0.03 and 0.22 s of the trigger time in the low- and high-energy ranges for the *Swift*-BAT and the *Fermi*-GBM detectors. Given the sampling frequency and the duration, the frequency space is defined in the range 4–125 Hz. **Top**: the periodogram for each detector (blue and green, respectively) and the summed signal from both detectors (grey). The periodogram of the background noise from the 10 s preceding the precursor is shown with a fine solid line. A 21.6 Hz signal is marked with a red dashed vertical line. No signal at 21.6 Hz is seen in the low energy data. **Bottom**: the individual periodogram for each detector and the summed signal from both detectors. The 21.6 Hz signal is marked with a red dashed line. Background noise level from the preceding 10 s is shown.

4.1.2 Short-time Fourier transform

To produce an STFT we start by 'Hanning a signal' at each bin centroid (Blackman & Tukey 1958), then use a Fourier transform to produce a PSD for each step. As the windowed data extend to include the full precursor time-series, for each step, there is an $n - 1$ overlap for each window function. Due to the short duration of the precursor, this ensures that there are sufficient data within each interval for a Fourier transform, and the window function biases the signal to the periodicity in the signal for the data centred on each time-step. Using the full series will 'smear' out any apparent periodicity, especially at times where the data are at approximately the background level and the window function includes significant signal from the brightest precursor period, $\sim$0.0–0.1 s. The total

[3]Fermi-GBM data.

[4]For the short-duration precursor we found the constant detrend via SCIPY.SIGNAL returned the same results for the *Fermi*-GBM data as using the GDT-CORE tools to remove the background trend, based on a $\gtrsim 20$ s interval of background data before the burst trigger time. The same constant detrend method was used with the *Swift*-BAT precursor data, returning a signal with zero counts line consistent with the *Fermi*-GBM data.

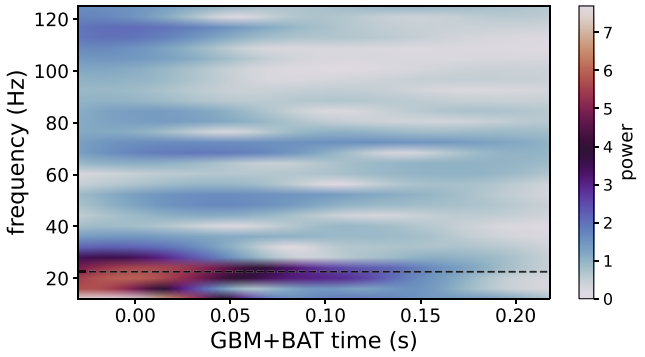

Figure 2. The combined *Fermi*-GBM and the *Swift*-BAT signal for the 'all' data analysed between 10 and 125 Hz via an STFT. The colour-map indicates the relative power density at the given time. The dashed black line indicates the location of the quasi-periodic 22.5 Hz signal from Xiao et al. (2024).

signal for the 'all' band from *Swift*-BAT and *Fermi*-GBM is shown in Fig. 2 – the detrended and combined signal is passed through an STFT and the resulting spectrogram is plotted. The candidate 22.5 Hz frequency (Xiao et al. 2024) is indicated via a horizontal dashed black line.

STFTs for band 1, 2, 3, 4, and 'all' are applied individually to the light curves from *Fermi*-GBM and *Swift*-BAT. The signal, raw (black) and detrended (blue), spectrogram, and an LS periodogram for each band are shown in Figs 3 and 4 for GBM and BAT, respectively.

4.2 Periodogram results

Fig. 1 shows both the 'low' (top panel) and 'high' (bottom panel) data periodograms via an LS. The precursor data between −0.03 and 0.22 s are shown via a thick solid line, where blue is the *Fermi*-GBM, green is *Swift*-BAT, and grey is the combined signal. The background noise level via a periodogram of the −10 to −5 s data is shown as fine solid lines – the precursor signal is seen clearly above the background levels. The 'low' data have a smaller power than that of the 'high' data – in both cases, the highest signal power is seen at frequencies $\lesssim 30$ Hz. The low-frequency signal peaks at ~ 4 Hz, which is coincident with the inverse of the precursor duration, $t_{\rm dur} \sim$ 0.2–0.25 s. A further look at the light-curve and LS periodogram for the precursor is included in the Appendix A, Fig. A1. The LS periodogram of the 'high' data reveals a signal at 21.6 Hz. A PSD via Welch's method for *Fermi*-GBM and *Swift*-BAT data is shown in Appendix A, Fig. A2, where the QPO signal and several other periodic features are identified and indicated via vertical red lines/shaded boxes.

The STFT for the 'all' data, shown in Fig. 2, indicates a ~ 22.5 Hz feature where a stronger signal is seen for the time period $-0.05\ {\rm s} \lesssim t - t_0 \lesssim 0.15$ s. The STFT for *Fermi*-GBM and *Swift*-BAT data for bands 1, 2, 3, 4, and 'all' are shown in Figs 3 and 4. The top row of each figure shows the individual precursor light curves for the raw and detrended data; the background noise level is indicated by a shaded region that encompasses the mean and plus/minus standard deviation for the 10 s data preceding the precursor. The middle row contains the STFT for each band; the colour-bar on the right indicates the relative power at each time-step and frequency. The bottom row is the LS for each band with the noise signal from the background data preceding the precursor – the location of the QPO at 22.5 Hz is shown with a black vertical dashed line in the LS panels, and a white horizontal dashed line in the STFT panels. The data in band 1 do not have a peak coincident with the proposed QPO. The STFT and LS panels show that the power is dominant at low frequencies, < 10 Hz – this is due to the precursor duration as discussed above.

Using the 'high' band data periodogram in Fig. 1, the fraction of the total precursor power in the QPO signal between 18 and 26 Hz is 13.2 per cent. For this fraction, we assume that all of the low-frequency data are due to the precursor duration and fractional periods, while any red noise is insignificant – see discussion in Appendix A.

4.3 Pulse profiles

Individual GRB pulses can be modelled following Norris et al. (2005):

$$N(t) = \frac{A\lambda}{e^{(\tau_1/t + t/\tau_2)}} \qquad t > 0, \tag{14}$$

where t is the time after a zero time, t_0, and A is the amplitude of the pulse; $\lambda = e^{(2\mu)}$ with $\mu = \sqrt{\tau_1/\tau_2}$, and τ_1 and τ_2 define the exponential rise and decay time-scales of the pulse.

The photon count data (see the top panels in Figs 3 and 4) exhibit multiple pulses within the $\Delta t \sim 0.25$ s duration of the precursor. Xiao et al. (2024) gave the minimum variability time-scale (MVT) for the precursor of $\tau_m = 15 \pm 2$ ms, which is longer by a factor of ~ 2 than the MVT of the main burst complex, $\tau_m = 8.5 \pm 0.8$ ms, which is interpreted by Xiao et al. (2024) as evidence for the precursor's different origin from the main burst.

To model the ~ 0.2 s precursor, we sample the data within a 0.25 s window and use one of three pulse profile models:

(i) **Single pulse:** a singular pulse given by equation (14).

(ii) **Pulse + sinusoid:** a singular pulse given by equation (14) and sinusoidal oscillation given by

$$N_\omega(t) = \frac{A}{10} \sin\left(2\pi\, \nu_\omega [t - x/\nu_\omega]\right), \tag{15}$$

where ν_ω is the quasi-periodic oscillator frequency, and x is a variable between 0 and 1.

(iii) **Multipulse:** pulses that have a profile that follows equation (14) but with a periodic occurrence frequency ν_ω; the number of pulses within the profile is given by the integer $\mathbb{Z} = 0.25\nu_\omega$, and the zero-point for each pulse is $t_0(\mathbb{Z} > 1) = t + \tau_2 - [\mathbb{Z} - 1]/\nu_\omega$. The amplitude, A, for the pulses is given by

$$A e^{-6\pi x(\mathbb{Z}-1)/\nu_\omega}, \qquad 0 \le x \le 1. \tag{16}$$

We fit these models to the summed *Fermi*-GBM and *Swift*-BAT data in the 'high' band. This energy range is motivated by the consistency between the LS periodograms for our low- and high-energy bands, and the STFT of the individual bands, both indicating that the candidate QPO is only seen at energies $\gtrsim 25$ keV (see Figs 1, 3, and 4).

The combined data in the 'high' range are time-normalized to the peak time, t_p, and given a zero-point $t_0 = t_p - 0.02$ s. As any negative counts from Model (ii) are unphysical, and because the pulse models (i) and (iii) can only predict positive counts, we adjust the counts level by the minimum of the background, ensuring that all have a positive value. The background in gamma-ray observations has multiple and complex potential components (Biltzinger et al. 2020); as we are focused on a very short time window, the background has been determined using the data before the precursor event – this shows a linear trend with small fluctuations ± 2 photons per 4 ms bin. As

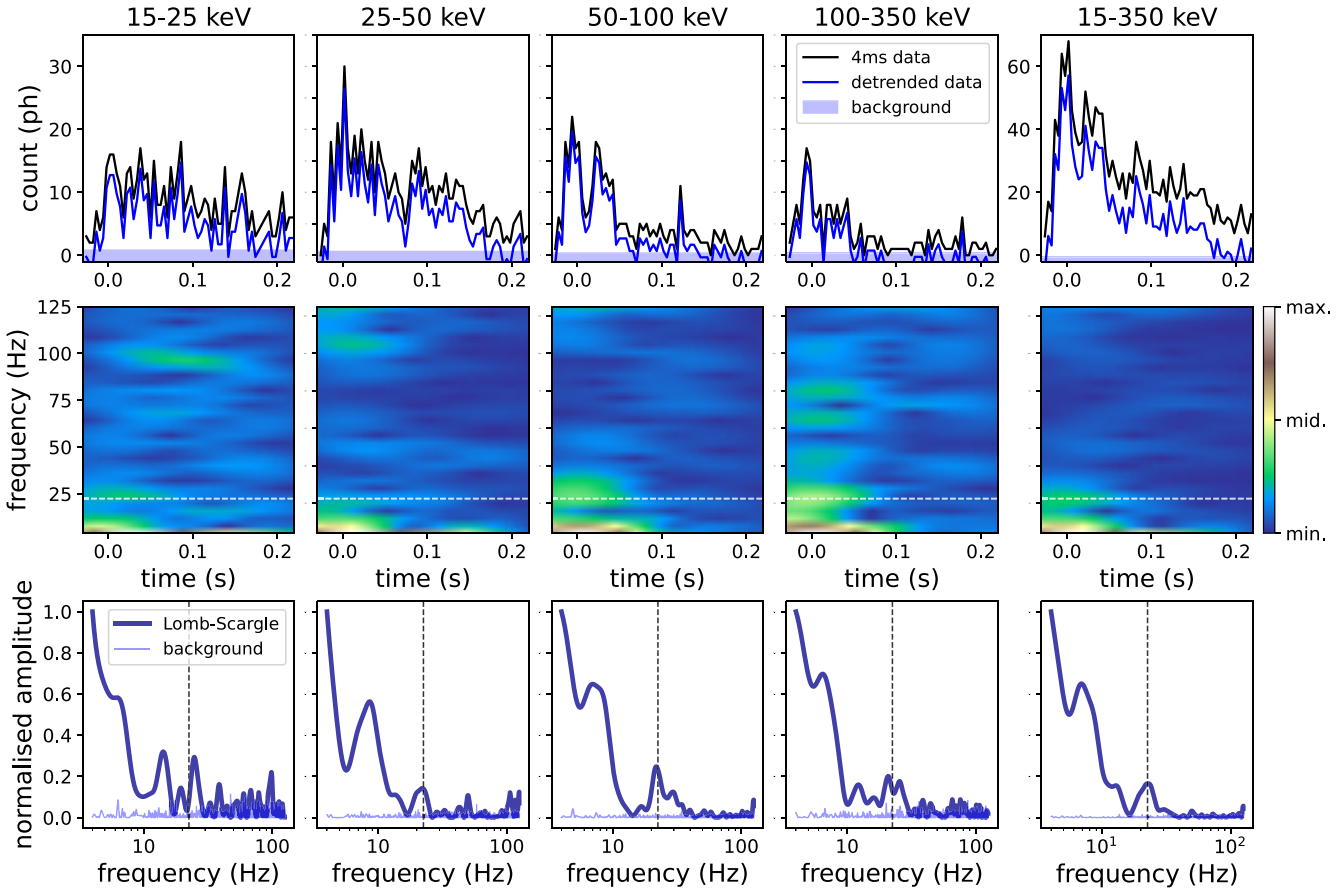

Figure 3. **Top row**: light curves at band 1, 2, 3, 4, and all binned at 4 ms from the *Fermi*-GBM observations of the pre-cursor, −0.03–0.22 s. Raw data shown with a black line, and the detrended data are shown in blue. **Middle row**: the STFT for each band over the precursor duration. The colour-scale corresponds to the amplitude of the signal at a given frequency and time relative to the amplitude range for each band. The horizontal dashed white line indicates the candidate QPO at 22.5 Hz. **Bottom row**: the LS periodogram at each band for the series shown in the top panel. Amplitudes are normalized individually. The position of the proposed 22.5 Hz quasi-periodic signal is shown with a dashed black line. The background signal level from the preceding 10 s is shown as a fine solid line.

the precursor signal drops to levels comparable to the background within 0.2–0.25 s, the positive offset allows all counts within the 0.25 s duration of the precursor data to contribute to the fit for all models. To fit models (i)–(iii) to the data, we use NESSAI (Williams, Veitch & Messenger 2021; Williams, Veitch & Messenger 2023), a nested sampling algorithm for Bayesian inference that incorporates normalizing flows. We marginalize over the fit parameters in the ranges listed in Table 2. We fix $A = 73.3$ for consistency with the peak of the combined data – for Model (ii), the fixed model amplitude, A, is reduced as the oscillation signal can contribute an additional 10 per cent to the peak counts.

The posterior distributions from the fits for the three pulse models to the precursor data are shown in the top panel of Fig. 5, and the corner plots for each are in Appendix B. We plot 400 randomly selected samples from each model posterior. Model (i) is shown in green; Model (ii) in orange; and Model (iii) in purple. The horizontal dashed teal line indicates the background trend level and the shaded region the background uncertainty.

The middle panel of Fig. 5 shows the difference between the model counts and the data. The black dashed line indicates the data – model equality, and the uncertainty due to Poisson noise and background fluctuations are shown as a grey shaded region. Each of the models (i–iii) are shown with the same colours as in the top panel.

The posterior parameters' median and 1σ credible interval are listed in Table 3. We fit these models using a narrow prior for the QPO, motivated by the periodogram analysis showing a consistent signal across two instruments at 22.5 Hz and no significant features other than those at $\lesssim 10$ Hz; however, Model (iii) sits against the lower boundary, indicating that this model, if unconstrained by the appropriate prior, will extend beyond the nominal lower bound. The model simplicity and fixed parameters (e.g. amplitudes, rise and decline time-scales, damping rate) all introduce uncertainty and the posteriors give the 'best fit' for these data versus the individual models. The log ratio for each model, based on the Bayes factor comparison and shown in Table 3, gives an indication for which of these models is preferred. However, the true model is likely to be significantly more complicated than the simplified global trends of models (i)–(iii).

A QPO in the range 20–25 Hz will produce $n \sim 5$–6 peaks within a 0.25 s precursor – for Model (iii) in Fig. 5, the number of peaks is $n = 5$; for Model (ii), the number of peaks is $n = 6$.

4.3.1 *Peaks and troughs*

Individual pulses within the precursor can be identified following Li & Fenimore (1996). Candidate peaks are found by isolating data

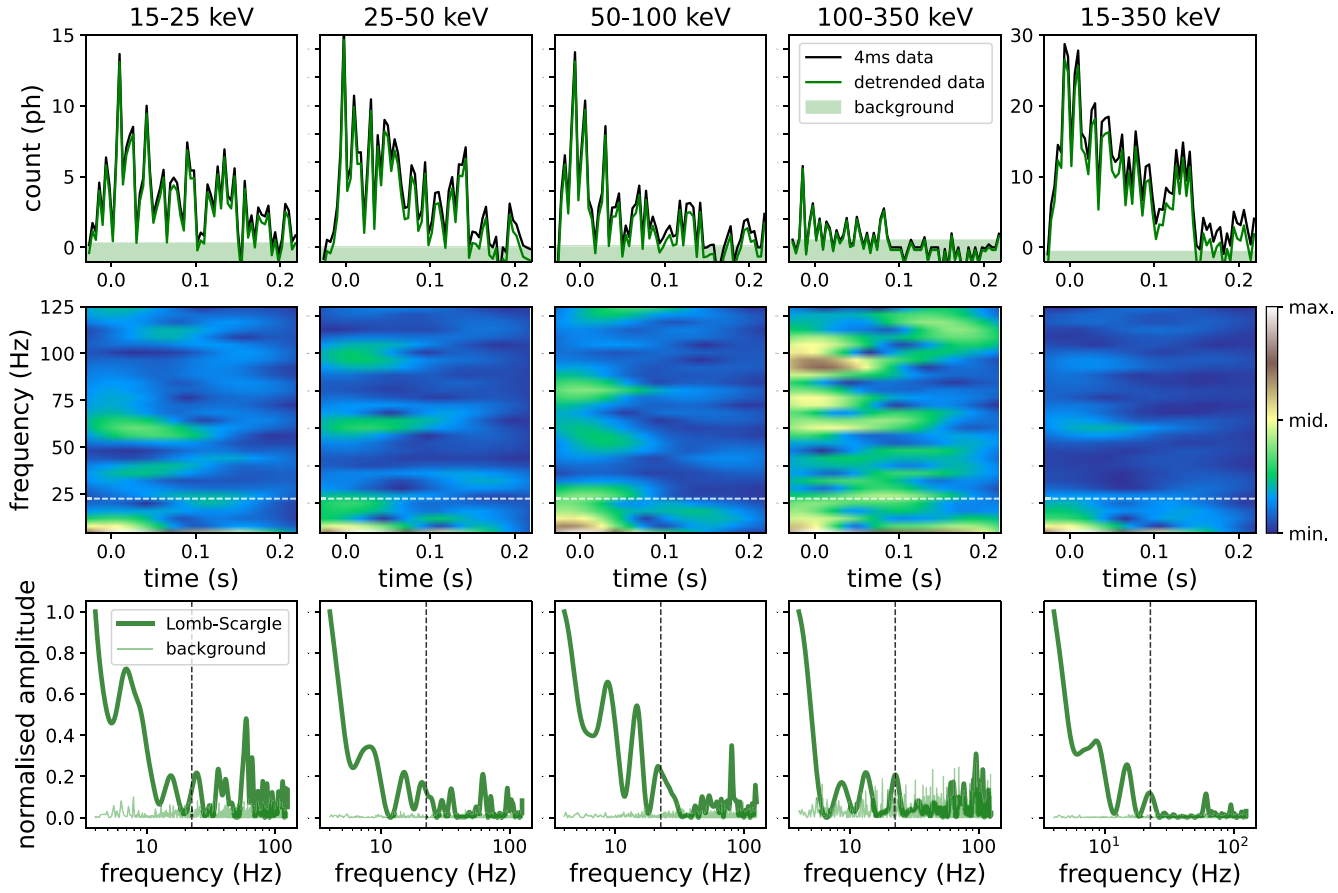

Figure 4. **Top row**: same as Fig. 3 but for the *Swift* -BAT data.

Table 2. Prior ranges for precursor pulse models (i)–(iii).

Model	τ_1 (ms)	τ_2 (ms)	x	ν_ω (Hz)
(i)	8–300	8–300	–	–
(ii)	8–300	8–300	0–1	20.0–30.0
(iii)	8–300	8–300	0–1	20.0–30.0
Distribution	log	log	linear	linear

points that are greater than both the preceding and the following data. However, this method will identify spurious data due to noise; to mitigate this, we identify peak counts that meet the condition

$$n_p - N_v\sqrt{n_p} \geq n_{1,2}, \tag{17}$$

with n_i being the counts at $(i = p)$ peak, $(i = 1)$ the data point before the pulse peak, and $(i = 2)$ the data point after peak; N_v is a factor in the range $3 \leq N_v \leq 5$ and accounts for noise within the data. Once the peaks, n_p, are located in this manner, then the troughs can be identified by finding the minimum counts between consecutive peaks.

The bottom panel of Fig. 5 shows peaks and troughs in the 'high' band light curve. There are 17 peaks identified, giving an average variability time-scale of 14.7 ± 2.0 ms over the 0.25 s duration, which is consistent with the MVT found by Xiao et al. (2024) at 15 ± 2 ms. However, the MVT between the precursor peaks is 8 ms, twice the bin size and therefore the smallest peak-to-peak time-scale possible with this data set. This short peak-to-peak time-scale highlights the challenges in peak and trough identification, where it is likely that we have overestimated the number of true peaks. By averaging a number of data points preceding and trailing a candidate peak, an improved estimate can be determined. By averaging six data points each side, we find peaks and troughs with gold circles in Fig. 5. The number of gold circle peaks is nine, which is fewer than the simplest peak finding method but still more than found via fitting QPO models to the data. As a candidate QPO exists within the raw data, the variability that results in the higher number of peaks in the peak-to-peak analysis, beyond any likely statistical variations (e.g. the complex at ~ 150 ms), is indicative of intrinsic variability related to the emission mechanism of GRBs.

Although significant (Xiao et al. 2024), the precursor has a lower signal-to-noise ratio than the data used in Li & Fenimore (1996) to formulate the peak-to-trough identification algorithm (equation 17), which may limit the effectiveness of the unique peak identification here. To test the effectiveness of the peak-to-tough algorithm, we generate a comparable FRED pulse with a background ± 2.5 counts and Gaussian counting noise, then fit our algorithm. The original Li & Fenimore (1996) peak-to-trough finds 15 peaks, mostly clustered around the late tail, with three peaks between t_0 and 0.1 s. There are a further four candidate peaks in this same time window. Our modified method, averaging counts for six points before and after, returns six peaks – two at the maximum of the pulse at < 0.05 s, and four in the tail at > 0.13 s. No periodicity is apparent in the yellow peaks for our fake pulse – we therefore consider our later estimate of nine peaks within five pulses to be more indicative of the true variability above noise within the precursor.

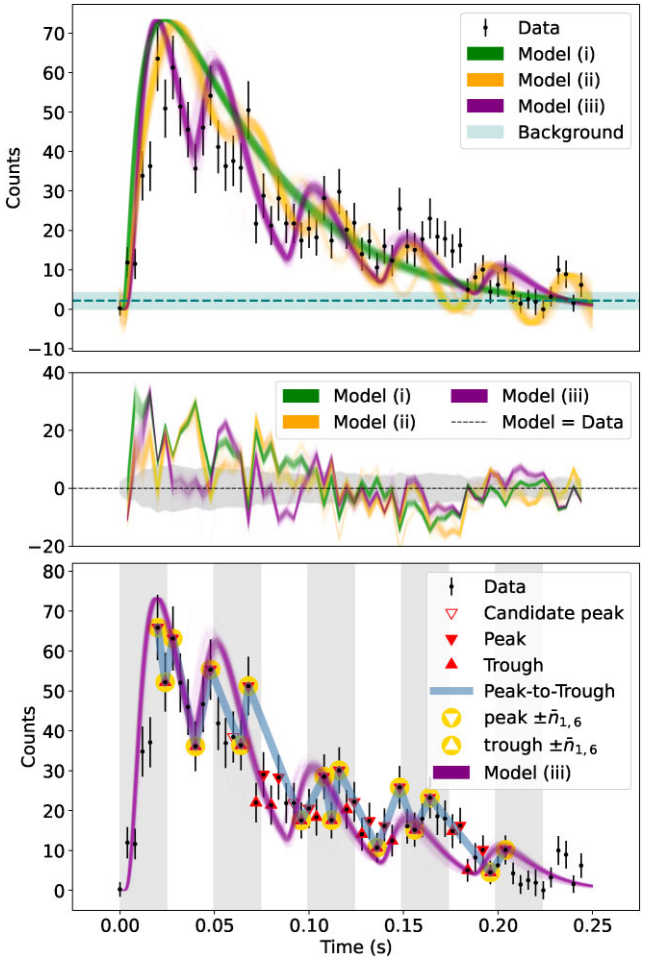

Figure 5. Top: the combined *Fermi*-GBM and *Swift* -BAT GRB background-subtracted 'high' band data, normalized by the peak time and offset by 0.02 s to give a zero-point for the start of the pulse. Three models fit to the data: green is Model (i) – the posterior sample for a single pulse profile; orange is Model (ii) – the posterior sample for a single pulse plus a sinusoidal signal; and purple is Model (iii) – a posterior sample from a multipulse model with periodic timing. **Middle:** the difference between the data and the model. The black dashed line is a difference of zero. The grey shaded region indicates the range of the data's error bars, and the combination of the background noise and data uncertainty. The difference line for each model is shown with the corresponding model colour. **Bottom:** the peaks and troughs identified via equation (17) (red down, up triangles, with two early candidate peaks identified with hollow triangles), the pulse trend identified via the peaks and troughs (slate blue), and Model (iii) overlaid (purple). The grey vertical panels indicate half the QPO period – equivalent to the engine duty cycle.

5 DISCUSSION

The peaks and troughs identified in the bottom panel of Fig. 5 provide an insight into the variability of the signal. The inclusion of the noise term weakens the identification of peaks when one or both neighbouring data points are similar in amplitude. We average six data points before and after a candidate peak, and use equation (17). The number of identified peaks then changes from 17 to 9, and the median variability time-scale between these peaks is $\sim 15 \pm 2$ ms. The MVT from the peak-finding method remains at 8 ms, the minimum set by twice the time bin duration. Such a short MVT implies a high Lorentz factor via pair opacity arguments, with an 8 ms time-scale putting a lower limit at $\Gamma \gtrsim 80$ where we assume all of the kinetic energy is radiated as $\gamma-$rays – an unrealistic 100 per cent efficiency within the precursor.

Table 3. Posterior sample median and 1σ credible interval for the model parameters fit to the data. The lower section gives the $\log \mathcal{B}$, of the ln Bayes factor for the comparison between the evidences for each of the models. A positive value prefers the model listed to the left of the row, while a negative value indicates a preference for the model in the column header. The best-fitting model is indicated via bold text in the row and column headers.

Model	τ_1 (ms)	τ_2 (ms)	x	ν_ω (Hz)
(i)	10^{+1}_{-1}	56^{+2}_{-2}	–	–
(ii)	13^{+1}_{-1}	55^{+2}_{-2}	$0.52^{+0.06}_{-0.06}$	$24.29^{+0.60}_{-0.45}$
(iii)	$\mathbf{26^{+3}_{-2}}$	$\mathbf{15^{+0}_{-1}}$	$\mathbf{0.56^{+0.02}_{-0.02}}$	$\mathbf{20.13^{+0.14}_{-0.08}}$
$\log \mathcal{B}$	(i)	(ii)	(iii)	
(i)	0	−9.248	−22.357	
(ii)	0.248	0	−13.109	
(iii)	**22.257**	**13.109**	**0**	

Internal shock model: Where an individual pulse is assumed to be the result of relativistic shell collisions (e.g. Kobayashi et al. 1997), two shells are required to produce a single pulse. Each shell has a characteristic mass and Lorentz factor – we label these M_i and Γ_i, respectively. A collision between a fast and a slow shell, as a result of the different shell velocities, results in a merged shell. If we assume an inelastic collision, then the resulting Lorentz factor will be

$$\Gamma_m = \sqrt{\Gamma_f \Gamma_s \left[\frac{\Gamma_f M_f + \Gamma_s M_s}{\Gamma_s M_f + \Gamma_f M_s}\right]}, \tag{18}$$

where the subscripts m, f, and s indicate the merged, fast, and slow shell.

The number of discrete peaks for a burst complex is equivalent to one less than the minimum number of shells, or overdensities, required to produce the signal via internal collisions: $n_{\rm shells} \geq n + 1$. For shell collisions to occur in this model, the leading shells will be slower than the trailing shells, where $\tilde{t}_i$ is the ejection time for each shell ($i = 1...n_{\rm shells}$); then, $\tilde{t}_{n_{\rm shells}} = 0$ (i.e. all earlier shells have $\tilde{t}_i < 0$). The width of each shell, l_i, corresponds to the duration of each engine activity episode as l_i/c and the size of the inner engine must be $< \min l_i$. The distance between the shells is given by $L_i = R_i - R_{i+1} - l_{i+1}$, where $R_i = -\tilde{t}_i c(1-\Gamma_i^{-2})^{1/2}$, is the radius of the initial, inner edge of a shell. Then, L_i/c is equivalent to the duration of the engine's zero or low activity.

We assume that for an individual shell, the rise time corresponds to the reverse shock crossing time-scale of the fast (catching) shell following a collision, where the time-scale is $\tau/(1+z)$. The size of the shell is therefore

$$l_{i+1} = \frac{\tau c}{(1+z)}(\beta_{i+1} - \beta_{rs}), \tag{19}$$

where τ corresponds to τ_1 in equation (14), $\beta = \sqrt{(1-\Gamma^{-2})}$, and the subscript 'rs' refers to the reverse shock quantity. The reverse shock properties can be found from the merger of two shells, where the Lorentz factor of the merged shells is given by equation (18), with $M_s, \Gamma_s \equiv M_i, \Gamma_i$ and $M_f, \Gamma_f \equiv M_{i+1}, \Gamma_{i+1}$. Then, the reverse shock Lorentz factor is (Kobayashi et al. 1997)

$$\Gamma_{rs} = \sqrt{\frac{1 + 2\Gamma_m/\Gamma_{i+1}}{2 + \Gamma_m/\Gamma_{i+1}}}, \tag{20}$$

leading to $\beta_{rs} = \sqrt{1-\Gamma_{rs}^{-2}}$.

The MVT, τ_m, of the prompt emission provides a lower limit on the Lorentz factor: $\Gamma \gtrsim 80(E/10^{51}\mathrm{erg})^{1/5}(\tau_m/0.1\mathrm{s})^{-2/5}$, where E is the jet isotropic equivalent total energy (Lamb & Kobayashi 2016). The precursor has an isotropic γ-ray energy $E \sim 6.97 \times 10^{48}$ erg (Xiao et al. 2024) – however, the energy in γ-rays is only a small fraction of the total energy. The multiple internal shock collision model is classically found to result in low efficiencies, < 0.1 (Mochkovitch, Maitia & Marques 1995); however, see Kobayashi & Sari (2001) for the case of ultra-efficient internal shocks. For an efficiency of ~ 0.02, the total jet energy would be of the order of $E_{\mathrm{total}} \sim 3.5 \times 10^{50}$ erg, and using $\tau_m/(1+z) = 14(7.4)$ ms, the Lorentz factor is $\Gamma > 142(175)$. A low efficiency of $\eta \sim 0.02$ implies that the range of Lorentz factors across the precursor outflow is a factor ~ 2 (Kobayashi et al. 1997).

It is not trivial to analytically estimate the parameters for a minimum of 10 shells colliding in series to give the resultant pulse profile seen with Model (iii). We therefore use the number of unique pulses identified by the the peaks-to-trough algorithm, using $n = 9$ (yellow points in Fig. 5). The QPO is then the result of a periodic jet on/off time-scale wherein the 'on' cycle ejection of impulsive shells is stochastic. We note that there are approximately two peaks within each of the pulses of Model (iii) for the light curve, suggesting an average of three shells ejected per 'on' cycle.

The energy per pulse is proportional to the number of photons, and each pulse has an identical profile as equation (14) in terms of the parameters τ_1 and τ_2 (thus ensuring the periodicity) but a unique amplitude, A_i; then, the energy per pulse scales as $E_i = E_{\mathrm{total}} A_i / \sum_i A_i$. Each pulse has $n \geq 2$ shells, and the energy for each shell is identical such that $E_i/n = S_i$, where $i = 1, \ldots n$. Each of the shells within an engine cycle will collide and merge within the half-period, $P/2 \sim 25$ ms, of the on/off cycle. As the observed γ-ray emission is only produced when shells collide, the assumed number of shells per pulse is the minimum; in reality, there can be many more components that do not collide in this period or which carry insufficient energy to create a bright pulse. Each pulse complex preserves the periodicity of the engine activity despite the stochastic nature of the unique pulse shells – this is evidenced in the alignment of identified peaks with the grey 'on' cycles shown in the bottom panel of Fig. 5.

We sub-divide the peaks and troughs into distinct interval groups. Each group has a temporal separation between neighbouring peaks of $\Delta t \geq 20$ ms. The peaks naturally split into five clusters of $n \sim 2$ peaks. We use these to infer the various energy, mass, and Lorentz factor requirements to recreate the observed precursor phenomenology. We assume that the number of shells per pulse is $n_{\mathrm{shells}} = n + 1$, and that the kinetic energy within each pulse is distributed equally among the individual shells. The shell minimum Lorentz factor, Γ_i, is determined in the same way as we previously found the minimum Lorentz factor of the precursor given the MVT; however, here we use the time from the preceding trough to peak (i.e. the rise time) and the individual shell energy.[5] The shell collision times are assumed to be the preceding trough time, the shell width is given by equation (19) and β_{rs} is found with equation (20), and mass is the isotropic equivalent assuming $M_i = E_{i,\mathrm{shell}}/(\Gamma_i c^2)$. Quantities are listed in Table 4.

[5]For merged shells, the total energy is the sum of the two merging shells minus the energy converted to internal energy. The energy conversion efficiency for our system is of the order of 10^{-4}–10^{-2} and so is not evident in the listed values in Table 4.

Table 4. Individual peaks identified via the yellow markers in the bottom panel of Fig. 5 tend to line up with the half-QPO period shown with grey panels. Pulses are separated by $24.7/(1+z)$ ms, and individual peaks correspond to the collision of two shells; thus, each pulse has $n+1$ shells. We assume the initial shell within each pulse is the first shell collision product for each pulse. The initial Lorentz factors are based on the minimum Γ, given the shell energy and the time-scale from previous trough to peak. All time-scales are in the rest frame.

Pulse	n_{peak}	$t_{0,\mathrm{collision}}$ ms	Γ	E_{shell} $\times 10^{49}$ erg	M_{shell} $\times 10^{-7}\,\mathrm{M}_\odot$	l/L
1	$0+1$	0	86	10.0	6.48	–
	2	22	163	5.0	1.70	0.63
2	$0+1$	37	112	6.0	3.02	0.60
	2	59	148	3.0	1.14	0.14
3	$0+1$	89	87	3.7	2.38	0.39
	2	104	134	1.8	0.78	0.57
4	$0+1$	126	78	2.2	1.60	0.53
	2	145	92	1.1	0.68	0.80
5	$0+1$	182	90	2.0	1.26	0.22

For each pulse, the first peak is the result of the collision of shells 0 and 1 within that pulse complex. The individual Lorentz factors for each shell, across all pulse complexes, have values such that no shell from an earlier pulse will be caught by the merged shell (equation 18) in the following pulse.

The decaying peak luminosity structure is a distinct feature of the precursor, and may be related to the damping of the mechanism responsible for the periodicity. This analysis demonstrates that the precursor's temporal phenomenology can be recreated with a simple baryonic shell collision model for GRB prompt emission. Via the multiple shell modelling, and by summing the individual shell masses in Table 4, the total mass within the precursor is $1.90 \times 10^{-6}\,\mathrm{M}_\odot$, if the emission were isotropic. Using the jet half-opening angle[6] $\theta = 3.^\circ27$ from the afterglow modelling in Rastinejad et al. (2022) and assuming bipolar jets, the mass in the precursor is $2.99 \times 10^{-9}\,\mathrm{M}_\odot$; assuming a jet-to-accretion efficiency of $\eta \sim 0.01$, the accretion rate for the precursor would be $\simeq 2.99 \times 10^{-7}\,\mathrm{M}_\odot\mathrm{s}^{-1}$, well within the constraints expected for a low-energy jet. If we assume an accretion rate $\sim 10^{-2}\mathrm{M}_\odot\mathrm{s}^{-1}$, then the accretion-to-jet efficiency for the precursor is $\eta \sim 10^{-5}$, consistent with the $NN - T_c$ and $NN - T_s$ models from Gottlieb et al. (2023), where the T indicates an initially toroidal magnetic field.

Implications of the precursor Lorentz factor: The rapid variability within the precursor, and the apparent periodicity when the data are compared with the best-fitting model (see the top and middle panel of Fig. 5) requires a minimum Lorentz factor $\Gamma \gtrsim 100$. Such a rapid outflow is inconsistent with precursor emission as a result of shock or cocoon breakout, where the light curve will be smoother and the Lorentz factor low: $\Gamma \sim 2$ to 10 (e.g. Wang et al. 2007; Gutiérrez et al. 2025). However, for long GRBs, precursor emission *has* been associated with shock or cocoon breakout (e.g. Ramirez-Ruiz et al. 2002; Nakar & Piran 2017), while short GRB precursors show little difference to the main burst complex (Troja et al. 2010) and are likely to have an engine origin. Given that GRB 211211A is associated with a candidate kilonova and defines a 'new' class of long, merger origin GRBs (Gompertz et al. 2023), the precursor emission in such merger origin systems will reflect early engine activity, as for short GRBs.

[6]The precursor outflow may have a different opening angle than that determined by the afterglow model, which we use here for convenience and lack of better information.

For a merger, the ejecta envelope that the jet has to 'drill' through is significantly smaller than the case of a collapsing massive star (Bromberg et al. 2012), and given the asymmetric nature of merger ejecta, the polar direction is expected to be relatively free of mass at early times – low-density ejecta in the polar directions would barely resist jet penetration, and any energy dissipated via early activity will produce precursors phenomenologically similar to the GRB main burst complex. The turbulent nature of early accretion following a neutron star merger provides ideal conditions for periodicity driven by instabilities within the disc that couple to a jet.

5.1 Black hole engine case

The engine size from the MVT is $\tau_m c \lesssim 2.4 - 4.5 \times 10^8$ cm, and $\approx 10 - 100 \times r_{\rm disk}$ for a neutron star merger. From the peak-to-trough analysis we find variability on a 4 ms time-scale (equal to the bin size, suggesting the true variability minimum is shorter); in the rest frame this results in an engine size $\lesssim 1100$ km, or 1.1×10^8 cm. Using the more conservative MVT, if the emission has its origin within a jet with a bulk Lorentz factor $\Gamma \gtrsim 140$, then the dissipation radius will be at $R_d \lesssim \Gamma^2 \tau_m c \sim 4.5 - 8.8 \times 10^{12}$ cm, and consistent with the expectation for GRB prompt emission.

Periodicity within a jet origin precursor suggests that the jet is coupled to the precession mechanism. In the case where the jet is powered by the Blandford–Znajek mechanism (Blandford & Znajek 1977), a QPO from LT precession of the accretion disc will have an oscillation frequency of the order of the inverse gravitational time, $t_g = GM_\bullet/c^3$. Where the QPO frequency is the inverse of the dynamical time $t_{\rm dyn} = \sqrt{r^3/GM_\bullet}$, with $t_{\rm dyn} > r/c$, the jet powering mechanism will be Blandford–Payne (Blandford & Payne 1982).

The mass range for the black hole engine is assumed to be between BH prompt collapse threshold (Sarin & Lasky 2021), $M_\bullet \gtrsim (3/2) M_{\rm TOV} \sim 3.4\,{\rm M}_\odot$, where $M_{\rm TOV} \simeq 2.25$ is the Tolman–Oppenheimer–Volkoff mass (Fan et al. 2024), and $M_\bullet \lesssim 4.5\,{\rm M}_\odot$, though we extend the black hole mass limit to $6.0\,{\rm M}_\odot$ to include black hole neutron star merger scenarios. For the LT precession at $22.5(1+z)$ Hz, and at a given radius, the required black hole spin $0.3 \leq \chi \leq 0.9$, equation (1), is shown in Fig. 6. The time-scale and radius for a 22.5 Hz QPO from a $\chi > 0.3$ black hole in this mass range is $100 \leq t \leq 150\,\mu$s and $30 \leq r \leq 45$ km, respectively. From Fig. 6, the LT effect at the QPO frequency can exist if the radius of the precession is ~ 5 to $9\,r_g$. This is consistent with the disc just beyond the innermost stable circular orbit for a rotating ($\chi = (0.3,\ 0.9)$) black hole – $r_{\rm ISCO} \sim (4.9,\ 2.3)\,r_g$. It is also potentially indicative of a disc tear due to early warping as a result of the LT precession (Nealon et al. 2015).

Among the alternative black hole disc origins for the QPO, many have periodicity due to Keplerian motion. Such oscillations include acoustic p modes, orbital resonances, and blobs within the disc. For discoseismology, g modes are comparable to p modes at large radial distances (i.e. the outer disc) where $N_{BV}/\kappa \sim 1$. For the inner radius, this ratio is typically $N_{BV}/\kappa > 1$, and the g-mode frequency will be higher than that of the p mode, which is equivalent to the Keplerian frequency.

We plot the Keplerian frequency for black hole mass and disc radius of our system in Fig. 7. The oscillation frequency ν_ϕ of Keplerian type oscillators scales with radius as $\propto r^{-3/2}$, with $\nu_\phi \sim 12$ kHz at a radius of r_g, ~ 2 kHz at the ISCO, and decreasing further to $\nu_\phi \sim 100$ Hz at 100 km (see Fig. 7). For the epicyclic frequencies (equation 7), using our parameter space, the radial epicyclic frequency at the observed QPO corresponds to distances

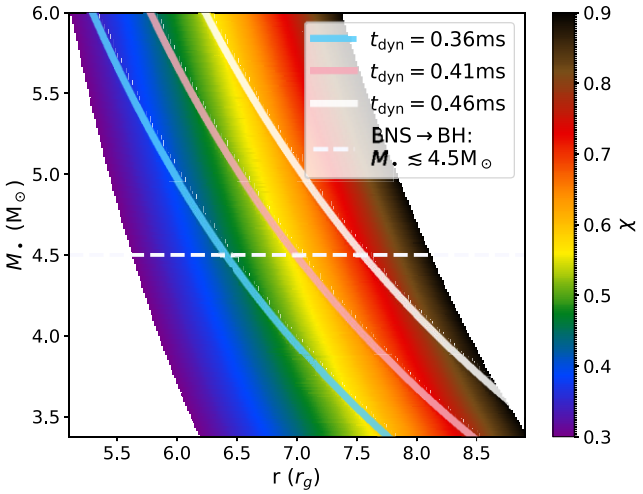

Figure 6. The black-hole spin for LT precession at $22.5(1+z)$ Hz shown with the colour-map, for a disc radius of $5.1 \leq r/r_g \leq 8.9$ as a factor of the gravitational radius, $r_g = GM_\bullet/c^2$ (and equivalent to $t_g = GM_\bullet/c^3$), and mass $3.38 < M_\bullet/{\rm M}_\odot < 6.00$. The solid contours are lines of constant dynamical time, $t_{\rm dyn} \simeq \sqrt{r^3/GM_\bullet}$. The horizontal white dashed line indicates the approximately maximum black hole mass following a binary neutron star merger, set at $2 \times M_{\rm TOV}$.

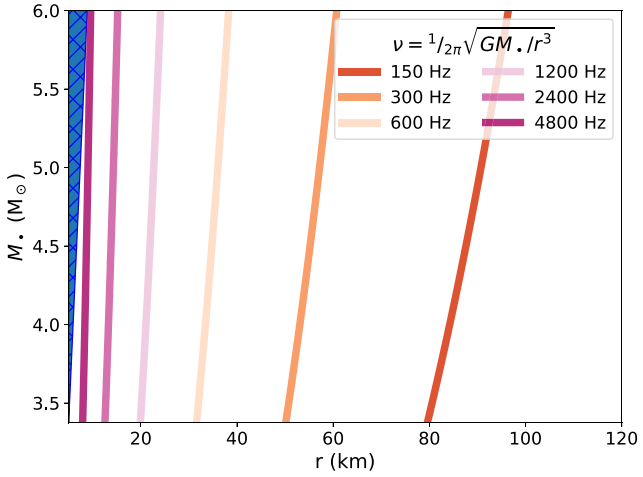

Figure 7. Given the black hole mass and radius within the disc, the QPO from the Keplerian frequency ranges from 10^2 to several 10^3 Hz, well beyond the 22.5 Hz of the observed QPO. The blue shaded hatched region gives the lower limit on the radius, $r = r_g(M_\bullet)$.

around $\gtrsim 90\ r_g \sim 590$ km, and vertical oscillations at a radius $\gtrsim 290$ km. When the epicyclic frequencies form integer ratios, such as $\nu_\theta/\nu_r = 3/2$, resonances can amplify the oscillatory modes, producing QPOs. Given the mass range of the system, the resonant radius has a lower limit $r > 1800$ km, and located beyond the edge of the disc. Additionally, the frequency in the 3:2 resonance is below the observed QPO at $\nu_{3:2} \sim 1.9 : 1.3$ Hz. The periastron precession frequency will be at the observed QPO, $\nu_{\rm low} \sim 22.5$ Hz for a radius of ≈ 450 km. Orbital resonances at the QPO frequency take place beyond the scale of the disc system from a merger.

For MHD MRI oscillations, the frequency is shown in Fig. 8. For the MHD oscillations, based on the Alfvén wavelength, there is parameter space for a 22.5 Hz QPO from the black hole system. Fig. 8 indicates this viable parameter space, notably the region to

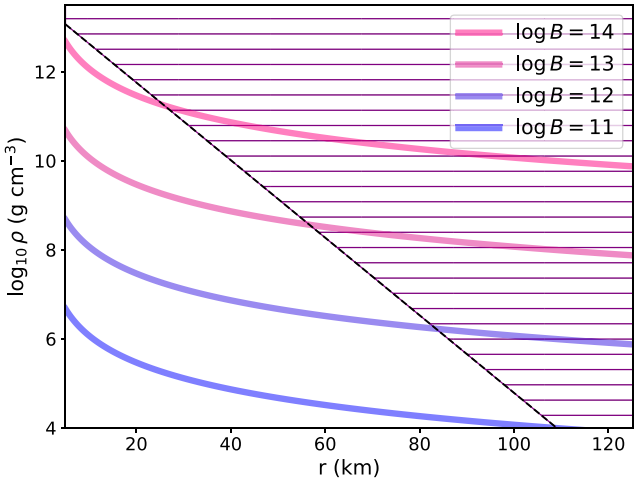

Figure 8. Parameter space and QPO within a BH disc given MHD instability scenarios. MHD or MRI oscillations, the white region indicates the potential parameter space for a $(1+z)$ 22.5 Hz QPO from a black hole accretion disc. Lines of constant B-field are shown with coloured contours. The horizontal hashed region is above the expected disc density (Kawaguchi, Fujibayashi & Shibata 2025).

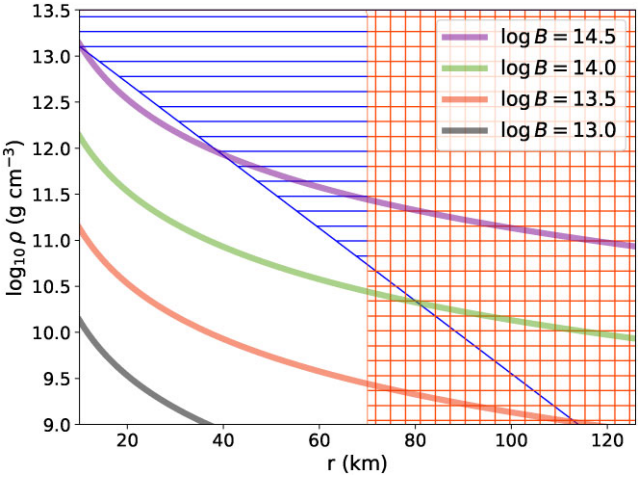

Figure 9. The magnetic field strength required for a QPO from Alfvén waves at $(1+z)$ 22.5 Hz, with the radial distance (within an accretion disc) and the corresponding density (from the solution to equation 22). The coloured contours indicate dex $B-$field values as given in the legend. The orange grid region lies beyond the maximum Alfvén radius, and is excluded. The blue striped region lies beyond the maximum density profile for the accretion disc and is also excluded.

the lower left of the lined zone – for a 22.5 Hz QPO, the required magnetic field is $10^{11}\,\mathrm{G} \lesssim B \lesssim 10^{14}\,\mathrm{G}$, with higher disc densities requiring a stronger magnetic field and a smaller radial distance to the instability responsible for the QPO. An MRI within the inner disc regions of a turbulent accretion disc, the 'dead zone', will result in episodic accretion giving an apparent duty cycle for the engine (Masada et al. 2007; Masada & Shibata 2009).

It is worth noting that, although we consider only a QPO within the disc, MHD instabilities can also occur at the base of, or within, the jet. The order of magnitude for the conditions required by such instabilities is similar to that for the inner disc case, and requires a length-scale comparable to r_g.

5.2 Magnetar engine case

The constraints on the maximum size of the engine from the rise times of the modelled pulses [$\tau_1 = 26/(1+z)$ ms for the preferred Model (iii)] are $\tau_1 c \lesssim 7200$ km. This length-scale is nearly two orders of magnitude larger than the expectation for a neutron star merger disc system, typically $\lesssim 200$ km (e.g. Rosswog et al. 2024).

If the observed QPO is coupled to the magnetar spin, then we can infer a spin period of $P \sim 44/(1+z)$ ms. Such spin–QPO coupling would place the oscillation at the co-rotation radius within the disc, $r_c = (GMP^2/(2\pi)^2)^{1/3} \approx 270$ km. Alternatively, the Alfvén frequency, $\nu_A \equiv \nu_{\rm QPO}$ (assuming the Alfvén frequency sets the QPO frequency), within a magnetosphere places a limit on the magnetic field strength. A limit on the maximum radial extent for Alfvén wave oscillations is the Alfvén radius, $r_{\rm A} = \mu^{4/7}(GM)^{-1/7}(3M_{\rm disk}/t_\nu)^{-2/7}$, where $\mu = BR^3$ is the magnetic moment (and constant at all radii above the surface for a dipole); $M_{\rm disk} \sim 0.1\,\mathrm{M}_\odot$ is the mass of the disc (Hotokezaka et al. 2013), and $t_\nu = r_{\rm disk}/(\alpha c_s)$, where we fix the dimensionless viscosity parameter[7] as $\alpha \sim 0.1$ (King et al. 2007), and the sound speed is $c_s \leq c/\sqrt{3}$.

[7]Estimates of the value of α can vary (e.g. Starling et al. 2004; King et al. 2013; Martin et al. 2019).

The range of the required magnetic field strength for a QPO at the observed frequency, given the constraints on the radius and density of the plasma, is shown in Fig. 9, where the x-axis shows the range in radius, $1 < r\ (\times 10^6\ \mathrm{cm}) < 32$, and the y-axis shows the range in density, $9.0 < \log\rho\ (\mathrm{g\,cm^{-3}}) < 13.5$ (see e.g. figs 1 and 5 in Rosswog et al. 2024).

The maximum field strength of a magnetar, $B_{\rm max}$, is determined by equating the magnetic energy with the gravitational binding energy, resulting in a maximum limit on the magnetic field strength:

$$B_{\rm max} \sim \left(\frac{GM_{\rm TOV}^2}{r_m^4}\right)^{1/2}. \tag{21}$$

We find that our system never violates this limit.

In Fig. 9 we assume a surface radius $r_m \sim 11$ km, the magnetic field above the surface declines as $B \propto r^{-3}$ for a dipole field and the density profile within the disc scales with radius as $\rho(r) = \rho_0 e^{-r/r_m}\ \mathrm{g\,cm^{-3}}$. The dependence on the radius within the disc for a given $\nu_{\rm QPO}$ is then

$$\nu_{\rm QPO} = \frac{1}{r_A(r)}\frac{B}{\sqrt{4\pi\rho_0}}\left(\frac{r}{r_m}\right)^{-3} \mathrm{e}^{r/2r_m}. \tag{22}$$

If the QPO is coupled to the spin, the ~41 ms period is within the expected estimates for a neutron star merger remnant. For this case, the luminosity due to dipole radiation is (e.g. Gibson et al. 2017)

$$L_{\rm d} = \frac{\eta_d}{(1-\cos\theta)}\frac{\mu^2\nu_s^4}{6c^3}, \tag{23}$$

where η_d is the dipole radiative efficiency, θ is the half-opening angle of the emission cone or jet, and ν_s is the magnetar spin frequency.

For a QPO that has its origin in the Alfvén wave frequency, the spin frequency is related to the Alfvén frequency via a harmonic number, such that $\nu_A = H\nu_s$. The dipole luminosity will reduce for higher harmonics, given a fixed efficiency and magnetic moment. The observed precursor luminosity is $L = 2.53^{+0.06}_{-0.47} \times 10^{49}\,\mathrm{erg\ s^{-1}}$ and the beaming corrected luminosity is $L_j = 4.11 \times 10^{46}\,\mathrm{erg\ s^{-1}}$, where we use the jet half-opening angle from afterglow modelling in Rastinejad et al. (2022) (note that the precursor may have a different

opening angle to the jet responsible for the afterglow). The dipole luminosity (equation 23), beamed into a jet half-opening angle of $\theta_j = 3.^{\circ}27 = 0.057$ rad, is 4.2×10^{46} erg s^{-1}, where we assume an efficiency of $\eta_d \sim 0.02$, and is consistent with the precursor beaming corrected power. However, as dipole radiation requires a rigidly rotating neutron star, and occurs of the order of $\mathcal{O}$(10s), dipole luminosity is inconsistent with the precursor time-scale.

In the magnetar origin precursor scenario, if the lifetime is $\gtrsim 10$ s (i.e. a stable and long-lived magnetar), then dipole radiation should be seen in the kilonova – the bolometric luminosity will be higher and the light-curve peak time-scale marginally earlier than the case without a magnetar engine (see e.g. Sarin et al. 2022; Ai, Gao & Zhang 2025). The dipole radiation from a magnetar is an additional term that adds to the internal energy of the merger ejecta (see equation 9 in Sarin et al. 2022) and increases the total luminosity of the kilonova. The addition of dipole radiation from a few ms spin magnetar increases the kilonova luminosity by a factor $\sim$ (10–1000), where the spin frequency is related to the dipole power from the magnetar via $L_{\rm d} \propto \nu_s^4$. However, as our period is approximately a factor 10 larger than a classical ms magnetar, the total dipole luminosity will be approximately four orders of magnitude smaller. The power budget for injection into the ejecta is then of the order of $\mathcal{O}(10^{45}$ erg s$^{-1})$, and despite the efficiency for the injection of the dipole power $\xi \rightarrow 1$ at early times (Sarin et al. 2022), when compared to the power from radioactive decay of the order of $\mathcal{O}(10^{49}$erg s$^{-1})$, the spin-down contribution from such a long-lived and stable magnetar is negligible. The light curves for a $L_d = 10^{45}$ erg s^{-1} magnetar powered kilonova are shown explicitly in fig. 2 of Ai et al. (2025), where a comparison with a non-engine fed kilonova is made. For such a long-lived magnetar engine, a late radio transient would be expected from the emergence of the pulsar wind nebula (Omand, Kashiyama & Murase 2018; Omand, Sarin & Lamb 2025). Such a radio transient would be expected at $\gtrsim 100$ d post burst; however, such a transient remains elusive (Schroeder & Fong 2024).

A magnetar with a spin-down power on this order will contribute insignificantly to the kilonova light curve at 1–10 d. The kilonova following GRB 211211A was shown to be inconsistent with the expectation from a magnetar-powered transient (Rastinejad et al. 2022); however, their magnetar kilonova models assumed a dipole luminosity approximately three orders of magnitude larger. For a magnetar spin-coupled QPO, the oscillation radius is $\sim$300 km, and beyond the scale expected for a merger system. Alternatively, for magnetar cases where the QPO does not reflect the rotation frequency, our assumption for the magnetar spin should place it at few kHz (Sarin et al. 2022; Ai et al. 2025), which would add significantly to the kilonova on time-scales ruled out by the observations, for a long-lived and stable neutron star (Rastinejad et al. 2022). Thus, for a magnetar origin of the QPO, we require a spin on the same order as the QPO frequency to ensure a low dipole luminosity, and the QPO radius to be significantly smaller than the spin co-rotation radius. Although we cannot rule out a magnetar origin, the required properties for such a system are unusual.

If the precursor duration reflects the time-scale for a hypermassive neutron star (HMNS), then the end of the precursor and gap to the main burst complex could indicate the collapse to a black hole. In such a scenario, the total mass of the merger system should be $M_{\rm total} < 2.8\,{\rm M}_{\odot}$, and the mass ratio should be $q \gtrsim 1.3$ – where we adopt the magnetically arrested disc model to produce the long-duration GRB (see fig. 2 in Gottlieb et al. 2023). The required HMNS spin frequency would be 0.5 kHz $\lesssim \nu_s \lesssim$ 3.5 kHz, with a radius $\sim$ 20 km (Rosswog & Davies 2002), implying that if the engine is an HMNS, then the observed QPO will not be of co-rotation origin and will therefore not be tracing the remnant spin period. Similar to the case for co-rotation above, if the HMNS rotation is not linked to the QPO frequency, then the rotation is likely of the order of a few kHz. As an HMNS will collapse to a black hole on a relatively short time-scale, and the collapse can occur before the rotational energy is depleted (Bernuzzi 2020), then no energy will be deposited within the ejecta and the kilonova will be unlikely to deviate from the non-engine fed models. In the HMNS scenario, the QPO can be produced via Alfvén wave oscillations within the inner disc at 20–50 km (see Fig. 9).

A magnetar or HMNS central engine does not rule out the internal shock model presented in Table 4. For such an engine, the individual shells will be accelerated by the same jet launching processes as the black hole engine, where jets from accretion are ubiquitous in astrophysical systems. The periodicity of the signal, due to Alfvén oscillations, will be imprinted in the engine 'on' and 'off' cycles. The nature of the shell ejection within each 'on' cycle could be a function of the details of acceleration in early jet launching physics and we note that the average number of peaks per 'on' cycle is constant.

For GRB 211211A, where the duration of the main burst complex is significantly longer than expected for neutron star merger systems, the system may be more 'exotic' than the non-unity mass ratio model of Gottlieb et al. (2023), and may well be an indicator of a spiral armed accretion complex seen in simulations of neutron star mergers where only one of the stars carries a significant spin (Rosswog et al. 2024), or neutron star magnetar mergers (Gao et al. 2022). While such a scenario may seem at first sight far-fetched, it is worth remembering that the majority of observed neutron stars in globular clusters are millisecond pulsars. Based on observed systems, the study of Rosswog et al. (2024) suggests that a non-negligible fraction ($\sim$ 5 per cent) of merging systems can contain a millisecond pulsar.

Such mergers are predicted to produce a dominantly red kilonova with a weak or missing blue component; for the kilonova in GRB 211211A, a significant blue component was observed – although, it was not easily fit by kilonova models (Rastinejad et al. 2022). Hamidani et al. (2024) noted that the blue and the red kilonova components are inconsistent with each other and they propose that the blue component is due to thermal emission from shock-heated ejecta due to late engine activity. In this scenario, the kilonova in GRB 211211A is almost entirely red.

5.3 The QPO at energies >25 keV only

The data are split into two energy bands: low and high (see Table 1). The relatively narrow low range is motivated by spectral fits that include a thermal component, with a cut-off power law plus blackbody having a thermal peak at 7.7 and 13.3 keV for a pure blackbody (Xiao et al. 2024). The first second of GRB emission was shown to have a low-energy break at 21.0 ± 8.8 keV, when fit with two smoothly broken power laws, and a blackbody temperature of 14.6 ± 2.4 keV when a thermal component is included (Gompertz et al. 2023). In both cases, however, the thermal component is disfavoured when compared to a non-thermal model.

The 'high' and 'low' band periodograms in Fig. 1, as well as the spectrograms in Figs 3 and 4, show that the QPO at $\sim$ 22.5 Hz is dominant at energies $\gtrsim$ 25 keV. Despite the better fits for a purely non-thermal model (e.g. Gompertz et al. 2023; Xiao et al. 2024), given that the QPO is at energies > 25 keV, we suggest that the lack of QPO signal in the 15–25 keV band is due to the contribution of photospheric emission for the precursor.

6 CONCLUSIONS

We show that the candidate QPO is present in both the *Fermi*-GBM and the *Swift*-BAT data at energies > 25 keV via LS and STFT methods (see also PSD in Appendix A). By fitting a periodic light curve/pulse model to the precursor emission, we demonstrate that a periodic engine cycle is consistent with the QPO from the periodogram analysis, and that periodic GRB pulses are preferred over a simple sinusoidal oscillation. We further demonstrate, via an internal shock model based on shell collisions within the jet, the required minimum Lorentz factors for individual shells to produce the variability time-scale of the precursor. This analysis reveals a periodic engine duty cycle, responsible for the QPO, where the energy within each engine cycle is damped in comparison to the previous. For the precursor, internal shocks occur only within the shells ejected within each engine cycle – this preserves the periodicity of the engine within the emission and requires a rapid damping of the oscillation mechanism.

The minimum Lorentz factor from the pulse and peak-and-trough analysis requires values of the order of $\Gamma \sim 100$; such a high Lorentz factor is inconsistent with a shock-breakout scenario for the precursor emission. Via pulse peak-to-trough analysis, we find a minimum variability for the precursor shorter than the sampling time-scale, $\lesssim 4$ ms, and a mean variability time-scale similar to that found by Xiao et al. (2024), ~ 15 ms. The short variability time-scale for the precursor is consistent with an origin within a relativistic outflow/jet – an engine-driven jet episode precursor to the more efficient, or powerful, main burst complex. This suggests that the jet power within the precursor is coupled to the mechanism that produces the QPO. The appearance of the QPO at > 25 keV in the precursor indicates that an additional emission mechanism exists at energies < 25 keV. The contribution of emission from the jet photosphere at a temperature of few keV would mask the non-thermal, pulsed lower energy emission within the jet.

The periodic signal in the range 18–25 Hz contains 13.2 per cent of the precursor energy. If the total energy is $E_{\rm pre,iso} \sim 3.5 \times 10^{50}$ erg (where we have assumed an emission efficiency of $\eta = 0.02$, Section 5), then the QPO has an energy budget of $E_{\rm QPO} \sim 4.6 \times 10^{49}$ erg – if the emission is isotropic, and $E_{j,\rm QPO} \sim 7.5 \times 10^{46}$ erg for a bipolar jetted outflow with a narrow $\theta_j \sim 3.27$ deg ~ 0.057 rad half-opening angle, where $E_{j,\rm QPO} \propto \theta_j^2$. The observed luminosity of the precursor is $L \sim 2.5 \times 10^{49}$ erg s^{-1}, and $L_j \sim 4.1 \times 10^{46}$ erg s^{-1}; for QPO coupled directly to the dipole power, a QPO will have a luminosity of $L_{j,\rm QPO} \sim 5.4 \times 10^{45}$ erg s^{-1}. The opening angle used here is narrow when compared to the GRB population (however, see Salafia et al. 2023, for a comparable narrow angle for short-duration GRBs), where both long and short GRBs have a typical opening angle from afterglow jet-break modelling of $\theta_j \sim 5.7$ deg ~ 0.1 rad (Aksulu et al. 2022). This is approximately a factor $\sim 7/4$ larger than the value inferred for GRB 211211A (Rastinejad et al. 2022), and so, if the precursor has a wider opening angle than the main emission, the energetics will be a factor ~ 3 larger.

We consider the implications under the assumptions that the central engine is a black hole or a magnetar:

For a black hole central engine:

(i) LT precession at the disc inner edge requires a radius of 5–9 r_g dependent on black-hole mass and spin.

(ii) In the LT case, higher mass black holes $\gtrsim 4.5\,{\rm M}_\odot$ with a spin $\chi \lesssim 0.7$ result in smaller radial requirements, $r \lesssim 7 r_g$.

(iii) The duration and damping time-scale of the precursor is consistent with precession through a thin ring at the inner disc – such a ring can indicate a warped and torn inner accretion disc region.

(iv) Oscillation processes that work on Keplerian orbits cannot reproduce the observed QPO.

(v) MHD effects, such as MRI, can produce the observed oscillation. For inner disc oscillations, the disc density and the magnetic field are positively proportional, with disc densities of $\sim 10^{12}$ g cm^{-3} requiring $B \sim 10^{14}$ G.

(vi) Such MHD-driven oscillations may also occur within the jet.

(vii) For MHD oscillations, the damping time-scale can trace the jet–disc coupling efficiency, or the crossing time-scale for Alfvén waves set by the ratio of the disc height to wave velocity.

Where the jet and disc are coupled, and the QPO origin is LT of the inner disc, the smallest radial solutions $\lesssim 6\, r_g$ indicate a black hole mass of $M_\bullet \gtrsim 4\,{\rm M}_\odot$. A black hole mass in this range is unlikely to be the result of a binary neutron star merger, although such a system cannot be ruled out; we suggest that the analysis here points towards a black hole neutron star merger as the system progenitor (Davies, Levan & King 2005).

For a magnetar central engine:

(i) Where the QPO is directly coupled to magnetar spin period, the QPO will be at $\gtrsim$300 km, and beyond the scale of a merger disc, < 200 km.

(ii) Where the QPO is the result of MHD instabilities within the disc and set by a local Alfvén wavelength, then the QPO will be at ~ 20 km (or within the inner disc), for a disc density of $\sim 10^{12}$ g cm^{-3}. The required magnetic field strength is $1 \leq B/(10^{14}{\rm G}) \leq 3$ – and consistent with a magnetar (Aguilera-Miret et al. 2025).

(iii) If the engine is an HMNS, the spin frequency is of the order of kHz, and therefore the QPO cannot be coupled to the HMNS rotation.

For long-lived and stable magnetars, the dipole radiation will inject significant energy into the kilonova – such an engine-fed kilonova is not seen in the observations (Rastinejad et al. 2022; Hamidani et al. 2024). Where the QPO is the result of Alfvén oscillations within the inner disc, then a short-lived (~ 0.25 s) magnetar or HMNS cannot be ruled out. Neither can more exotic merger origins, such as a neutron star – pulsar within a globular cluster.

Although a magnetar or HMNS cannot be entirely ruled out, a black hole engine origin for the QPO is naturally explained via LT precession of the inner disc that is coupled to the jet at early times. For an early turbulent accretion disc, the jet and disc will align via torques induced by LT, or the Blandford–Znajek process – typically, the BZ process will dominate (Polko & McKinney 2017). The competing torques on the jet–disc system at early times can induce disc warping and tearing, where differential precession across a thin inner ring would reproduce the precursor time-scale and characteristic damping. The gap between the precursor and the main emission then reflects the time-scale for the bulk disc to commence rapid accretion, powering the main GRB jet. The gap time-scale will be equivalent to the dynamical time for the bulk accretion at the disc inner-edge.

ACKNOWLEDGEMENTS

We thank the anonymous referee for their insightful and helpful comments that have improved this work. GPL thanks Jillian Rastinejad for useful comments on an early draft, Siong Heng for fruitful discussions, Mery Ravasio for a crash-course introduction to *Fermi*-GBM data, and Samuel Tosh and Michael Hebden for inspiring

work on internal shock models during an undergraduate SURE summer internship at University of Leicester and a Royal Society funded summer undergraduate studentship at Liverpool John Moores University, respectively.

This work utilizes tools from SCIPY (Virtanen et al. 2020), GDTCORE (Goldstein, Cleveland & Kocevski 2024), NESSAI (Williams 2021), BILBY (Ashton et al. 2019), PRIDE-PALETTES (Gallinger 2020), HEASOFT (Blackburn 1995), MATPLOTLIB (Hunter 2007), and REDBACK (Sarin et al. 2024).

GPL, CMBO, and CT are supported by a Royal Society Dorothy Hodgkin Fellowship (grant nos. DHF-R1-221175 and DHF-ERE-221005). KLP acknowledges funding from the UK Space Agency. Dimple and BPG acknowledge support from STFC grant no. ST/Y002253/1. BPG acknowledges support from The Leverhulme Trust grant No. RPG-2024-117. IM acknowledges support from the Australian Research Council (ARC) Centre of Excellence for Gravitational Wave Discovery (OzGrav), through project number CE230100016. NS acknowledges support from the Knut and Alice Wallenberg Foundation through the 'Gravity Meets Light' project and by the research environment grant 'Gravitational Radiation and Electromagnetic Astrophysical Transients' (GREAT) funded by the Swedish Research Council (VR) under Dnr 2016–06012. SR has been supported by the Swedish Research Council (VR) under grant number 2020–05044 and by the research environment grant 'Gravitational Radiation and Electromagnetic Astrophysical Transients' (GREAT) funded by the Swedish Research Council (VR) under Dnr 2016–06012, by the Knut and Alice Wallenberg Foundation under grant Dnr. KAW 2019.0112, by Deutsche Forschungsgemeinschaft (DFG, German Research Foundation) under Gemany's Excellence Strategy – EXC 2121 'Quantum Universe' – 390833306 and by the European Research Council (ERC) Advanced Grant INSPIRATION under the European Union's Horizon 2020 research and innovation programme (Grant agreement No. 101053985). RS acknowledges support from Leverhulme Trust grant RPG-2023-240.

DATA AVAILABILITY

Data utilized are from public repositories, Swiftdata archive, and Fermi-GBM data products.

REFERENCES

Abbott B. P. et al., 2017, ApJ, 848, L12
Aguilera-Miret R., Christian J.-E., Rosswog S., Palenzuela C., 2025, preprint (arXiv:2504.10604)
Ai S., Gao H., Zhang B., 2025, ApJ, 978, 52
Aksulu M. D., Wijers R. A. M. J., van Eerten H. J., van der Horst A. J., 2022, MNRAS, 511, 2848
Armitage P. J., 2022, preprint (arXiv:2201.07262)
Ashton G., et al., 2019, ApJS, 241, 27
Bardeen J. M., Petterson J. A., 1975, ApJ, 195, L65
Barnes J., Metzger B. D., 2023, ApJ, 947, 55
Beniamini P., Wadiasingh Z., Hare J., Rajwade K. M., Younes G., van der Horst A. J., 2023, MNRAS, 520, 1872
Bernuzzi S., 2020, Gen. Relativ. Gravit., 52, 108
Biltzinger B., Kunzweiler F., Greiner J., Toelge K., Burgess J. M., 2020, A&A, 640, A8
Blackburn J. K., 1995, in Shaw R. A., Payne H. E., Hayes J. J. E., eds, ASP Conf. Ser. Vol. 77, Astronomical Data Analysis Software and Systems IV. Astron. Soc. Pac., San Francisco, p. 367
Blackman R. B., Tukey J. W., 1958, Bell Syst. Tech. J., 37, 185
Blandford R. D., Payne D. G., 1982, MNRAS, 199, 883
Blandford R. D., Znajek R. L., 1977, MNRAS, 179, 433
Bromberg O., Nakar E., Piran T., Sari R., 2012, ApJ, 749, 110
Burlon D., Ghirlanda G., Ghisellini G., Lazzati D., Nava L., Nardini M., Celotti A., 2008, ApJ, 685, L19
Burlon D., Ghirlanda G., Ghisellini G., Greiner J., Celotti A., 2009, A&A, 505, 569
Burrows D. N. et al., 2005, Science, 309, 1833
Chang X.-Z., Lü H.-J., Yang X., Chen J.-M., Liang E.-W., 2023, ApJ, 943, 146
Cheng K. S., Dai Z. G., 1996, Phys. Rev. Lett., 77, 1210
Chirenti C., Dichiara S., Lien A., Miller M. C., Preece R., 2023, Nature, 613, 253
Chirenti C., Dichiara S., Lien A., Miller M. C., 2024, ApJ, 967, 26
Cline D. B., Hong W., 1992, ApJ, 401, L57
Coppin P., de Vries K. D., van Eijndhoven N., 2020, Phys. Rev. D, 102, 103014
Davies M. B., Levan A. J., King A. R., 2005, MNRAS, 356, 54
Debnath S., Chattopadhyay I., Joshi R. K., 2024, MNRAS, 528, 3964
Dichiara S., Tsang D., Troja E., Neill D., Norris J. P., Yang Y. H., 2023, ApJ, 954, L29
Dimple, Misra K., Arun K. G., 2023, ApJ, 949, L22
Fan Y.-Z., Han M.-Z., Jiang J.-L., Shao D.-S., Tang S.-P., 2024, Phys. Rev. D, 109, 043052
Fernández R., Metzger B. D., 2016, Annu. Rev. Nucl. Part. Sci., 66, 23
Fryer C. L., Lloyd-Ronning N., Wollaeger R., Wiggins B., Miller J., Dolence J., Ryan B., Fields C. E., 2019, Eur. Phys. J. A, 55, 132
Gallinger C., 2020, Pride-palettes, https://github.com/cgallinger/pride_palettes (accessed 2 February 2025)
Gao H., Lei W.-H., Zhu Z.-P., 2022, ApJ, 934, L12
Gibson S. L., Wynn G. A., Gompertz B. P., O'Brien P. T., 2017, MNRAS, 470, 4925
Goldstein A., Cleveland W. H., Kocevski D., 2024, Gamma-ray Data Tools Core Package: version 2.1.1, https://github.com/USRA-STI/gdt-core (accessed 2 February 2025)
Gompertz B. P. et al., 2023, Nat. Astron., 7, 67
Gottlieb O. et al., 2023, ApJ, 958, L33
Guedes V., Radice D., Chirenti C., Yagi K., 2025, ApJ, 983, 88
Gutiérrez E. M., Bhattacharya M., Radice D., Murase K., Bernuzzi S., 2025, Phys. Rev. D, 111, 063031
Hamidani H., Tanaka M., Kimura S. S., Lamb G. P., Kawaguchi K., 2024, ApJ, 971, L30
Hotokezaka K., Kiuchi K., Kyutoku K., Muranushi T., Sekiguchi Y.-i., Shibata M., Taniguchi K., 2013, Phys. Rev. D, 88, 044026
Hu Y.-D., Liang E.-W., Xi S.-Q., Peng F.-K., Lu R.-J., Lü L.-Z., Zhang B., 2014, ApJ, 789, 145
Hübner M., Huppenkothen D., Lasky P. D., Inglis A. R., Ick C., Hogg D. W., 2022, ApJ, 936, 17
Hunter J. D., 2007, Comput. Sci. Eng., 9, 90
Kato S., 2001, PASJ, 53, 1
Kato S., Fukue J., 1980, PASJ, 32, 377
Kawaguchi K., Fujibayashi S., Shibata M., 2025, Phys. Rev. D, 111, 023015
King A. R., Pringle J. E., Livio M., 2007, MNRAS, 376, 1740
King A. R., Livio M., Lubow S. H., Pringle J. E., 2013, MNRAS, 431, 2655
Kobayashi S., Sari R., 2001, ApJ, 551, 934
Kobayashi S., Piran T., Sari R., 1997, ApJ, 490, 92
Koshut T. M., Kouveliotou C., Paciesas W. S., van Paradijs J., Pendleton G. N., Briggs M. S., Fishman G. J., Meegan C. A., 1995, ApJ, 452, 145
Kouveliotou C., Meegan C. A., Fishman G. J., Bhat N. P., Briggs M. S., Koshut T. M., Paciesas W. S., Pendleton G. N., 1993, ApJ, 413, L101
Kuan H.-J., Suvorov A. G., Kokkotas K. D., 2021, MNRAS, 508, 1732
Kumar S., Pringle J. E., 1985, MNRAS, 213, 435
Kunert N. et al., 2024, MNRAS, 527, 3900
Lamb G. P., Kobayashi S., 2016, ApJ, 829, 112
Lazzati D., 2005, MNRAS, 357, 722
Levan A. J. et al., 2024, Nature, 626, 737
Li H., Fenimore E. E., 1996, ApJ, 469, L115
Li L., Mao J., 2022, ApJ, 928, 152
Li X. J., Zhang Z. B., Zhang X. L., Zhen H. Y., 2021, ApJS, 252, 16
Li Y., Shen R.-F., Zhang B.-B., 2023, ApJ, 955, 98

Lipunova G. V., Gorbovskoy E. S., Bogomazov A. I., Lipunov V. M., 2009, MNRAS, 397, 1695
Lomb N. R., 1976, Ap&SS, 39, 447
Martin R. G., Nixon C. J., Pringle J. E., Livio M., 2019, New Astron., 70, 7
Masada Y., Shibata K., 2009, in Esquivel A. ,Franco J., García-Segura G. Dal Pino,de Gouveia E. M., Lazarian A., Lizano S., Raga A., eds, Magnetic Fields in the Universe II: From Laboratory and Stars to the Primordial Universe, Revista Mexicana de Astronomia y Astrofisica Conference Series, p. 163
Masada Y., Kawanaka N., Sano T., Shibata K., 2007, ApJ, 663, 437
Mei A. et al., 2022, Nature, 612, 236
Mészáros P., Ramirez-Ruiz E., Rees M. J., 2001, ApJ, 554, 660
Metzger B. D., 2020, Living Rev. Relativ., 23, 1
Mochkovitch R., Maitia V., Marques R., 1995, Ap&SS, 231, 441
Nakar E., Piran T., 2017, ApJ, 834, 28
Nappo F., Ghisellini G., Ghirlanda G., Melandri A., Nava L., Burlon D., 2014, MNRAS, 445, 1625
Narayan R., Piran T., Kumar P., 2001, ApJ, 557, 949
Nealon R., Price D. J., Nixon C. J., 2015, MNRAS, 448, 1526
Neill D., Tsang D., van Eerten H., Ryan G., Newton W. G., 2022, MNRAS, 514, 5385
Norris J. P., Nemiroff R. J., Bonnell J. T., Scargle J. D., Kouveliotou C., Paciesas W. S., Meegan C. A., Fishman G. J., 1996, ApJ, 459, 393
Norris J. P., Bonnell J. T., Kazanas D., Scargle J. D., Hakkila J., Giblin T. W., 2005, ApJ, 627, 324
Omand C. M. B., Kashiyama K., Murase K., 2018, MNRAS, 474, 573
Omand C. M. B., Sarin N., Lamb G. P., 2025, MNRAS, 539, 1908
Polko P., McKinney J. C., 2017, MNRAS, 464, 2660
Ramirez-Ruiz E., Celotti A., Rees M. J., 2002, MNRAS, 337, 1349
Rastinejad J. C. et al., 2022, Nature, 612, 223
Rosswog S., Davies M. B., 2002, MNRAS, 334, 481
Rosswog S., Diener P., Torsello F., Tauris T. M., Sarin N., 2024, MNRAS, 530, 2336
Salafia O. S., Ravasio M. E., Ghirlanda G., Mandel I., 2023, A&A, 680, A45
Sarin N., Lasky P. D., 2021, Gen. Relativ. Gravit., 53, 59
Sarin N., Omand C. M. B., Margalit B., Jones D. I., 2022, MNRAS, 516, 4949
Sarin N. et al., 2024, MNRAS, 531, 1203
Scargle J. D., 1982, ApJ, 263, 835
Schekochihin A. A., Cowley S. C., Dorland W., Hammett G. W., Howes G. G., Quataert E., Tatsuno T., 2009, ApJS, 182, 310
Schroeder G., Fong W.-f., 2024, American Astronomical Society Meeting Abstracts. p. 424.04D
Sejdić E., Djurović I., Jiang J., 2009, Digit. Signal Process., 19, 153
Starling R. L. C., Siemiginowska A., Uttley P., Soria R., 2004, MNRAS, 347, 67
Stone N., Loeb A., Berger E., 2013, Phys. Rev. D, 87, 084053
Sullivan A. G., Alves L. M. B., Márka Z., Bartos I., Márka S., 2024, MNRAS, 527, 7722
Suvorov A. G., Kokkotas K. D., 2020, Phys. Rev. D, 101, 083002
Tabone B., Rosotti G. P., Cridland A. J., Armitage P. J., Lodato G., 2022, MNRAS, 512, 2290
Török G., Stuchlík Z., 2005, A&A, 437, 775
Troja E., Rosswog S., Gehrels N., 2010, ApJ, 723, 1711
Tsang D., Read J. S., Hinderer T., Piro A. L., Bondarescu R., 2012, Phys. Rev. Lett., 108, 011102
Vaughan S., 2005, A&A, 431, 391
Virtanen P. et al., 2020, Nat. Methods, 17, 261
Wagoner R. V., 1999, Phys. Rep., 311, 259
Wang X.-Y., Li Z., Waxman E., Mészáros P., 2007, ApJ, 664, 1026
Wang J.-S., Peng F.-K., Wu K., Dai Z.-G., 2018, ApJ, 868, 19
Wang J.-S., Peng Z.-K., Zou J.-H., Zhang B.-B., Zhang B., 2020, ApJ, 902, L42
Waxman E., Ofek E. O., Kushnir D., 2025, ApJ, 984, 37
Welch P. D., 1967, IEEE Trans. Audio Electroacoust., 15, 70
Williams M. J., 2021, nessai: Nested Sampling with Artificial Intelligence, Zenodo, https://doi.org/10.5281/zenodo.4550693
Williams M. J., Veitch J., Messenger C., 2021, Phys. Rev. D, 103, 103006
Williams M. J., Veitch J., Messenger C., 2023, Mach. Learn.: Sci. Technol., 4, 035011
Xiao S. et al., 2024, ApJ, 970, 6
Yang J. et al., 2022, Nature, 612, 232
Yang X., Lü H.-J., Rice J., Liang E.-W., 2025, MNRAS, 537, 2313
Zhang B. et al., 2009, ApJ, 703, 1696
Zhang Z., Yi S.-X., Zhang S.-N., Xiong S.-L., Xiao S., 2022, ApJ, 939, L25
Zhong S.-Q., Dai Z.-G., Cheng J.-G., Lan L., Zhang H.-M., 2019, ApJ, 884, 25
Zhu J.-P., Wang X. I., Sun H., Yang Y.-P., Li Z., Hu R.-C., Qin Y., Wu S., 2022, ApJ, 936, L10
Zwicky F., 1974, Ap&SS, 28, 111

APPENDIX A: QPO SIGNAL DOUBLE CHECK

Fermi-GBM has multiple detectors – for this work we utilize the two channels, n2 and na, the two highest signal-to-noise data sets for this event. If the QPO is only present in one of these data sets, then the significance of the signal would be cast into doubt (note that Xiao et al. 2024 performed comprehensive significance tests for this signal in *Fermi*, *Swift*, and *Konus-Wind* data and confirmed the signal). However, we caution that the signal at 20–25 Hz is seen within independent telescopes – both *Swift* and *Fermi* here, and *Konus-Wind* in Xiao et al. (2024) initial discovery. The search in multiple detectors acts as a sanity check.

A1 Light-curve and LS periodogram

Here, we present the precursor light curves for 0.25 s of data from *Fermi*-GBM n1, n2, na and all 12 detectors merged, plus the *Swift*-BAT data, and the sum of the merged GBM plus BAT data; the combined bands data are the 'all' band (see Table 1 for band information), Fig. A1. The detector light curves and LS traces for n0, n3–n9, and nb are not shown, but are included in the'all' GBM.

The left panel of Fig. A1 shows the light curve data of the individual detectors and their sum, plus the other nine detectors from *Fermi*-GBM. The general FRED structure is maintained, and a clear 'on/off' periodicity is evident on a ~ 20 ms time-scale. The right panel shows the periodogram of this signal. The spectral power peaks at low frequencies, which is tempting to attribute to red noise – however, here the peak is that of the time series precursor duration, ~ 0.25 s and ~ 4 Hz. Utilizing a longer time series of data before and after (where after is more limited due to the main burst episode) reveals that the low-frequency power spectra levels off at frequencies below ~ 2 Hz, demonstrating behaviour inconsistent with red noise (Vaughan 2005) – long time series, lower frequency LS is not shown here.

A2 Welch's method

We further generate a PSD using Welch's method (Welch 1967) to confirm the results of the LS periodogram shown in the right panel of Fig. A1. The PSD is shown in Fig. A2. The locations of the expected periodicity are given: the pulse duration of ~ 0.2 s; the proposed QPO at 21.5 Hz; the apparent 'on' and 'off' cycle time of half the QPO period; and the sampling frequency MVT artefact are shown via red vertical lines and/or shaded regions. In the PSD plot, the signal above background noise is seen via broad spikes at frequencies that are generally coincident with the cases noted.

The various spectral features are consistent with an inspection of the time series data. A more detailed study of the precursor data is required to confirm the QPO significance (e.g. Hübner et al. 2022), which is beyond the scope of this work.

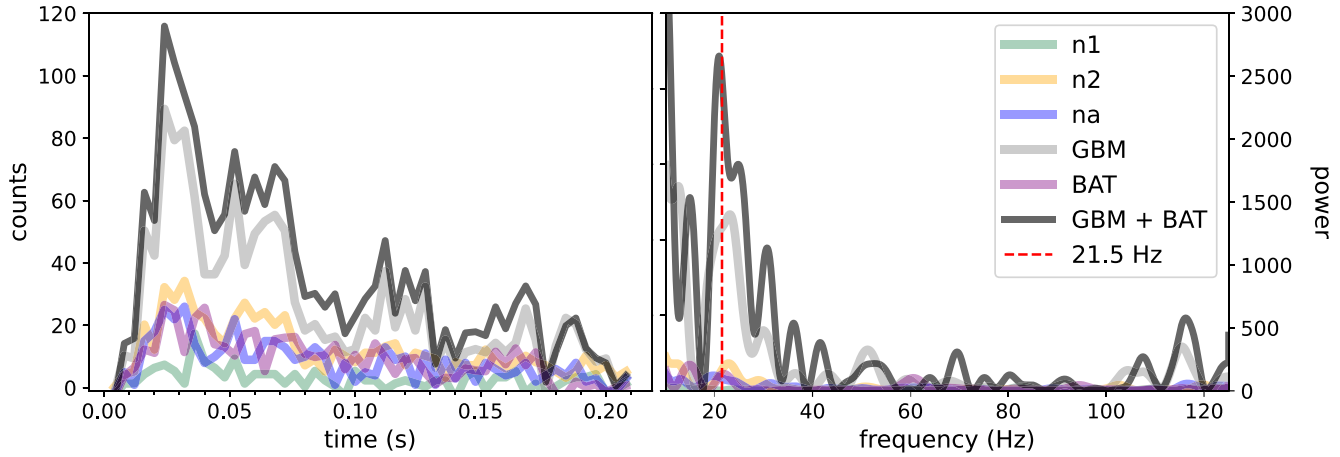

Figure A1. Left: light curves for n1, n2, na, all 12 GBM detectors summed, BAT, and GBM + BAT. **Right:** LS periodogram for each of the data sets shown in the left panel. A significant signal is seen at ∼ 20–25 Hz. The red dashed line marks the 21.7 Hz frequency identified in the main body. The spectrum is cut at the low end at < 10 Hz, which is dominated by the precursor duration.

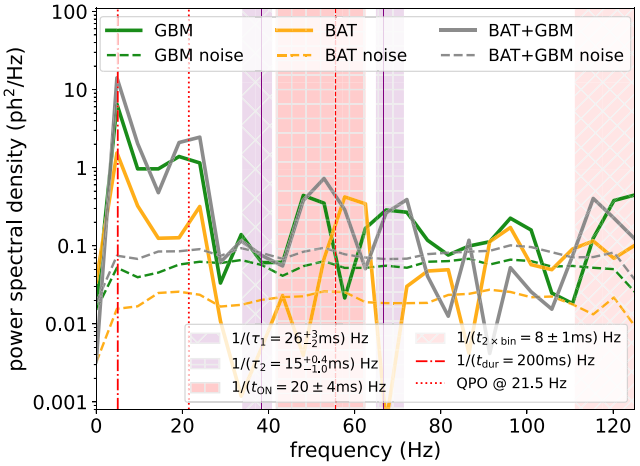

Figure A2. The PSD via Welch's method of the *Swift*-BAT, the *Fermi*-GBM na and n1, and the sum of the data. The noise trace is that of the background data for a duration of 10 s preceding the precursor. The vertical lines and shaded panels indicate various time-scales within the data: at ∼ 5 Hz the red dash–dotted line corresponds to the precursor duration, $t_{\rm dur} = 0.2$ s; the 21.5 Hz line is the candidate QPO; the shaded grid-hatched region at ∼ 55 Hz is the approximate 'ON' cycle duration for the engine; and the red cross-hatched region corresponds to the twice the sampling frequency. The two purple shaded regions are the model (iii) pulse rise and decline time-scales, with the shaded region at 38 Hz given by $\tau_1 = 26^{+3}_{-2}$ ms, and at 67 Hz the $\tau_2 = 15^{+0}_{-1}$ ms. Note also that the MVT found by Xiao et al. (2024) was 15 ms $\equiv \tau_2$.

APPENDIX B: POSTERIOR DISTRIBUTIONS

The model (i–iii) fits to the 'high' band combined *Fermi*-GBM and *Swift*-BAT precursor data, over a period of 0.25 s are shown graphically in Figs B1, B2, and B3.

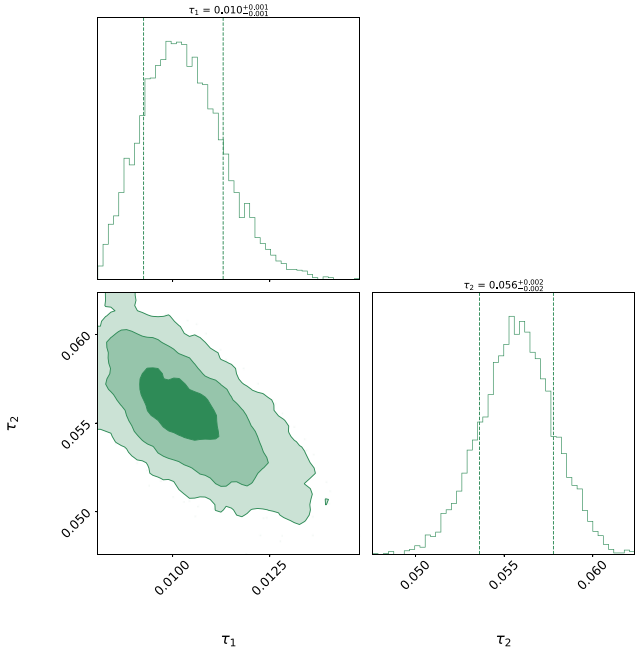

Figure B1. Model (i) – single pulse.

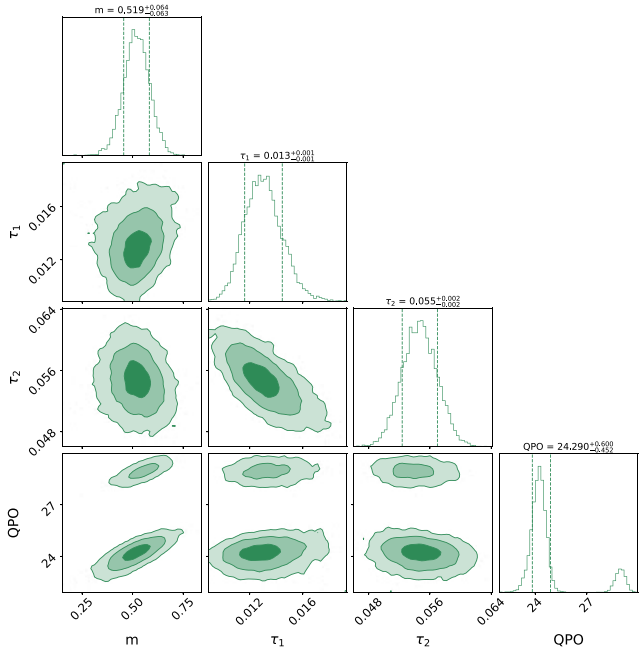

Figure B2. Model (ii) – single pulse plus sinusoid.

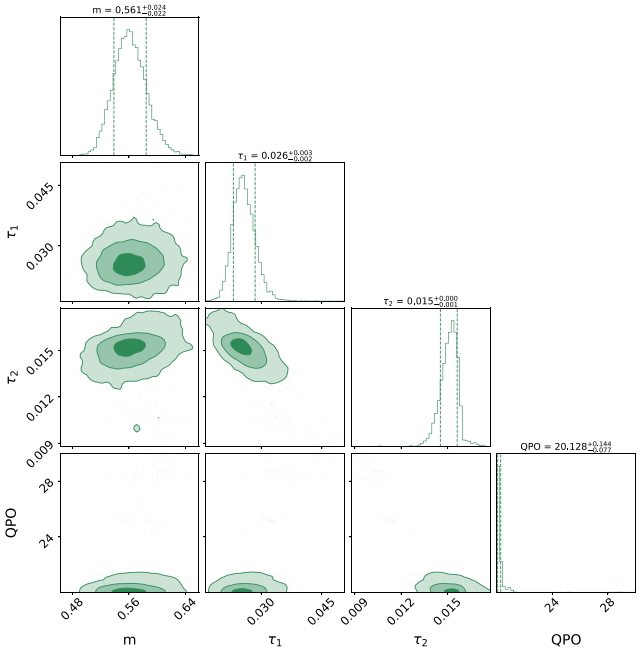

Figure B3. Model (iii) – multiple pulses with periodicity.

This paper has been typeset from a TEX/LATEX file prepared by the author.